Università degli Studi di Padova

Padua Research Archive - Institutional Repository

A study of quasi-elastic muon neutrino and antineutrino scattering in the NOMAD experiment

(Article begins on next page)

A study of quasi-elastic muon neutrino and antineutrino scattering in the NOMAD experiment

V. Lyubushkin[6,a], B. Popov[6,14], J.J. Kim[19], L. Camilleri[8], J.-M. Levy[14], M. Mezzetto[13], D. Naumov[6,7], S. Alekhin[25], P. Astier[14], D. Autiero[8], A. Baldisseri[18], M. Baldo-Ceolin[13], M. Banner[14], G. Bassompierre[1], K. Benslama[9], N. Besson[18], I. Bird[8,9], B. Blumenfeld[2], F. Bobisut[13], J. Bouchez[18], S. Boyd[20], A. Bueno[3,24], S. Bunyatov[6], A. Cardini[10], P.W. Cattaneo[15], V. Cavasinni[16], A. Cervera-Villanueva[8,22], R. Challis[11], A. Chukanov[6], G. Collazuol[13], G. Conforto[8,21,b], C. Conta[15], M. Contalbrigo[13], R. Cousins[10], D. Daniels[3], H. Degaudenzi[9], T. Del Prete[16], A. De Santo[8,16], T. Dignan[3], L. Di Lella[8,c], E. do Couto e Silva[8], J. Dumarchez[14], M. Ellis[20], G.J. Feldman[3], R. Ferrari[15], D. Ferrère[8], V. Flaminio[16], M. Fraternali[15], J.-M. Gaillard[1], E. Gangler[8,14], A. Geiser[5,8], D. Geppert[5], D. Gibin[13], S. Gninenko[8,12], A. Godley[19], J.-J. Gomez-Cadenas[8,22], J. Gosset[18], C. Gößling[5], M. Gouanère[1], A. Grant[8], G. Graziani[7], A. Guglielmi[13], C. Hagner[18], J. Hernando[22], D. Hubbard[3], P. Hurst[3], N. Hyett[11], E. Iacopini[7], C. Joseph[9], F. Juget[9], N. Kent[11], M. Kirsanov[12], O. Klimov[6], J. Kokkonen[8], A. Kovzelev[12,15], A. Krasnoperov[1,6], S. Kulagin[12], D. Kustov[6], S. Lacaprara[13], C. Lachaud[14], B. Lakić[23], A. Lanza[15], L. La Rotonda[4], M. Laveder[13], A. Letessier-Selvon[14], J. Ling[19], L. Linssen[8], A. Ljubičić[23], J. Long[2], A. Lupi[7], A. Marchionni[7], F. Martelli[21], X. Méchain[18], J.-P. Mendiburu[1], J.-P. Meyer[18], S.R. Mishra[19], G.F. Moorhead[11], P. Nédélec[1], Yu. Nefedov[6], C. Nguyen-Mau[9], D. Orestano[17], F. Pastore[17], L.S. Peak[20], E. Pennacchio[21], H. Pessard[1], R. Petti[19], A. Placci[8], G. Polesello[15], D. Pollmann[5], A. Polyarush[12], C. Poulsen[11], L. Rebuffi[13], J. Rico[24], P. Riemann[5], C. Roda[8,16], A. Rubbia[8,24], F. Salvatore[15], O. Samoylov[6], K. Schahmaneche[14], B. Schmidt[5,8], T. Schmidt[5], A. Sconza[13], M. Seaton[19], M. Sevior[11], D. Sillou[1], F.J.P. Soler[8,20], G. Sozzi[9], D. Steele[2,9], U. Stiegler[8], M. Stipčević[23], Th. Stolarczyk[18], M. Tareb-Reyes[9], G.N. Taylor[11], V. Tereshchenko[6], A. Toropin[12], A.-M. Touchard[14], S.N. Tovey[8,11], M.-T. Tran[9], E. Tsesmelis[8], J. Ulrichs[20], L. Vacavant[9], M. Valdata-Nappi[4,d], V. Valuev[6,10], F. Vannucci[14], K.E. Varvell[20], M. Veltri[21], V. Vercesi[15], G. Vidal-Sitjes[8], J.-M. Vieira[9], T. Vinogradova[10], F.V. Weber[3,8], T. Weisse[5], F.F. Wilson[8], L.J. Winton[11], Q. Wu[19], B.D. Yabsley[20], H. Zaccone[18], K. Zuber[5], P. Zuccon[13]

[1]LAPP, Annecy, France
[2]Johns Hopkins Univ., Baltimore, MD, USA
[3]Harvard Univ., Cambridge, MA, USA
[4]Univ. of Calabria and INFN, Cosenza, Italy
[5]Dortmund Univ., Dortmund, Germany
[6]JINR, Dubna, Russia
[7]Univ. of Florence and INFN, Florence, Italy
[8]CERN, Geneva, Switzerland
[9]University of Lausanne, Lausanne, Switzerland
[10]UCLA, Los Angeles, CA, USA
[11]University of Melbourne, Melbourne, Australia
[12]Inst. for Nuclear Research, INR, Moscow, Russia
[13]Univ. of Padova and INFN, Padova, Italy
[14]LPNHE, Univ. of Paris VI and VII, Paris, France
[15]Univ. of Pavia and INFN, Pavia, Italy
[16]Univ. of Pisa and INFN, Pisa, Italy
[17]Roma Tre University and INFN, Rome, Italy
[18]DAPNIA, CEA, Saclay, France
[19]Univ. of South Carolina, Columbia, SC, USA
[20]Univ. of Sydney, Sydney, Australia
[21]Univ. of Urbino, Urbino, and INFN, Florence, Italy
[22]IFIC, Valencia, Spain
[23]Rudjer Bošković Institute, Zagreb, Croatia
[24]ETH Zürich, Zürich, Switzerland
[25]Inst. for High Energy Physics, 142281, Protvino, Moscow Region, Russia

Abstract We have studied the muon neutrino and antineutrino quasi-elastic (QEL) scattering reactions ($\nu_\mu n \rightarrow \mu^- p$ and $\bar{\nu}_\mu p \rightarrow \mu^+ n$) using a set of experimental data collected by the NOMAD Collaboration. We have performed measurements of the cross-section of these processes on a nuclear target (mainly carbon) normalizing it to the total ν_μ ($\bar{\nu}_\mu$) charged-current cross section. The results for the flux-averaged QEL cross sections in the (anti)neutrino energy interval 3–100 GeV are $\langle \sigma_{\text{qel}} \rangle_{\nu_\mu} = (0.92 \pm 0.02(\text{stat}) \pm 0.06(\text{syst})) \times 10^{-38} \text{ cm}^2$ and $\langle \sigma_{\text{qel}} \rangle_{\bar{\nu}_\mu} = (0.81 \pm 0.05(\text{stat}) \pm 0.09(\text{syst})) \times 10^{-38} \text{ cm}^2$ for neutrino and antineutrino, respectively. The axial mass parameter M_A was extracted from the measured quasi-elastic neutrino cross section. The corresponding result is $M_A = 1.05 \pm 0.02(\text{stat}) \pm 0.06(\text{syst})$ GeV. It is consistent with the axial mass values recalculated from the antineutrino cross section and extracted from the pure Q^2 shape analysis of the high purity sample of ν_μ quasi-elastic 2-track events, but has smaller systematic error and should be quoted as the main result of this work. Our measured M_A is found to be in good agreement with the world average value obtained in previous deuterium filled bubble chamber experiments. The NOMAD measurement of M_A is lower than those recently published by K2K and Mini-BooNE Collaborations. However, within the large errors quoted by these experiments on M_A, these results are compatible with the more precise NOMAD value.

PACS 13.15.+g · 25.30.Pt

1 Introduction

A precise knowledge of the cross section of (anti)neutrino–nucleus quasi-elastic scattering process (QEL) is important for the planning and analysis of any experiment which detects astrophysical, atmospheric or accelerator neutrinos. The available measurements from early experiments at ANL [1–4], BNL [5–8], FNAL [9, 10], CERN [11–18] and IHEP [19–22] have considerable errors due to low statistics and a lack of knowledge of the precise incoming neutrino flux. Unfortunately, even within these large errors, the results are often conflicting.

This subject remains very topical. Recently several attempts have been made to investigate the QEL process

a e-mail: Vladimir.Lyubushkin@cern.ch

b Deceased

c Now at Scuola Normale Superiore, Pisa, Italy

d Now at Univ. of Perugia and INFN, Perugia, Italy

in the data collected by modern accelerator neutrino experiments (such as NuTeV [23], K2K [24, 25] and Mini-BooNE [26]). Unfortunately they have not clarified the situation again due to large errors assigned to their measurements. Dedicated experiments, such as e.g. SciBooNE [27] and MINERνA [28], are now being performed.

In the present analysis, we study both ν_μ and $\bar{\nu}_\mu$ QEL scattering in the data collected by the NOMAD Collaboration. The NOMAD detector was exposed to a wide-band neutrino beam produced by the 450 GeV proton synchrotron (SPS, CERN). A detailed description of the experimental set-up can be found in [29]. The characteristics of the incoming neutrino flux are given in [30].

The large amount of collected data and the good quality of event reconstruction in the NOMAD detector provide a unique possibility to measure the QEL cross section with a combination of small statistical and systematic errors. The data sample used in this analysis consists of about 751000 (23000) ν_μ ($\bar{\nu}_\mu$) charged-current (CC) interactions in a reduced detector fiducial volume. The average energy of the incoming ν_μ ($\bar{\nu}_\mu$) is 25.9 (17.6) GeV.

The merit of the current analysis is the possibility of keeping the systematic error relatively small. It takes advantage from three main factors: (1) the NOMAD detector is capable of selecting a sample of QEL events with a high purity and a good efficiency; (2) a simultaneous measurement of both two track and single track ν_μ QEL events allows one to constrain the systematics associated with nuclear reinteractions; (3) a wide energy range of the NOMAD neutrino beam allows one to perform a precise normalization to the well-known total (DIS) ν_μ CC cross section.

The paper is organized as follows. In Sect. 2 we give a brief review of the published experimental data on QEL (anti)neutrino scattering. The NOMAD detector and the incoming neutrino flux are briefly discussed in Sect. 3. In Sect. 4 we outline the MC modeling of signal and background events, emphasizing also the importance of nuclear effects. Section 5 is devoted to the selection of the QEL events; we describe the QEL identification procedure and compare the MC predictions with experimental data. The methods used to measure the QEL cross section and the phenomenological axial mass parameter M_A are the subjects of Sect. 6. The systematic uncertainties are summarized in Sect. 7. The results are presented in Sect. 8. Finally, a summary and discussion of the obtained results are given in Sect. 9.

More detailed information can be found in [31].

2 Review of existing experimental data on quasi-elastic (anti)neutrino scattering

Let us start with a brief review of existing experimental data on (anti)neutrino–nucleon QEL scattering.

A compilation of available data on the cross section measurement of the ν_μ and $\bar{\nu}_\mu$ quasi-elastic scattering off deuterium and other nuclei or composite targets (like freon, propane, liquid scintillator) as a function of the incoming neutrino energy has been made (see Figs. 17, 18 and 19). This study allowed one to conclude that the QEL cross section measured in different experiments can vary by 20–40%.

The existing data on (anti)neutrino QEL scattering come mostly from bubble chamber (BC) experiments. In general, these data suffer from small statistics. Moreover, results of several old experiments [12–14] have large systematic uncertainties due to the poor knowledge of the incoming neutrino flux and of background contamination in the selected events.

The total QEL cross section was recently measured in data collected by the NuTeV Collaboration [23]. The number of QEL events identified in their analysis are comparable with the total world data obtained in previous experiments. However, the results reported for the antineutrino case fall well outside the most probable range of values known today and hence, seem to exhibit a systematic shift.

Another intriguing subject in the study of the neutrino quasi-elastic scattering is the axial structure of the nucleon. We will skip here the details of the phenomenology of the hadronic current involved in the matrix element of the process (see Sect. 4.1 and [32]). But let us only remind the reader that for the region of low and intermediate 4-momentum transfer, Q^2, we can use a dipole parameterization for the axial form factor with only one adjustable parameter, the so-called axial mass M_A.

The M_A parameter describes the internal structure of the nucleon and should be the same both for neutrino and antineutrino experiments (if we assume the isotopic invariance of strong interaction). Therefore, it is convenient to compare experimental results in terms of the axial mass. There is, however, no theoretical basis for this form of the axial form factor. The use of an inappropriate parameterization could therefore lead to values of M_A that differ when extracted under different kinematical conditions.

There are two possible ways generally used to extract the M_A parameter from experimental data:

1. from the total QEL (anti)neutrino–nucleon cross section (the axial form factor is responsible for about 50–60% of the total QEL cross section);
2. from the fit of the Q^2 distribution of the identified neutrino QEL events.

In principle, these two procedures should give self-consistent results. However, the old bubble chamber experiments at ANL and CERN reported in general larger values of M_A based on the Q^2 fit than those obtained from the total cross-section measurements.

Results of the M_A measurements based on the Q^2 fit have been recently published by the K2K [24, 25] and Mini-BooNE [26] Collaborations. They are about 15% higher than the average of previous deuterium filled bubble chamber experiments. This disagreement is, however, just at about one sigma level because of the large systematic errors associated with the K2K and MiniBooNE measurements.

Let us note that the extraction of M_A from the Q^2 distribution fit is a more delicate issue than the QEL total cross section measurement.

In general, there are at least three aspects which can affect noticeably the M_A measurements:

1. The nuclear effects can distort the expected distributions of the measured kinematic variables (like the energy of the outgoing nucleon). The neutrino–nucleus interactions should be described by a theoretical model suitable for the considered neutrino energy region. This is important both for MC modeling in present-day neutrino experiments and for a proper interpretation of the results obtained earlier (with few exceptions for the deuterium filled bubble chambers).
2. The correct determination of the background contamination from both deep inelastic scattering and single-pion production in the selected events is important for experiments operating with intermediate and high energy neutrino beams.
3. The QEL reconstruction efficiency as a function of Q^2 for two-track events is not expected to be a flat function. It should drop both at small Q^2 due to the loss of low energy protons and at large Q^2 due to the loss of low energy muons. Effects which influence the efficiency of the low momentum particle reconstruction should be carefully taken into account in the MC modeling of the detector response.

Tables 1 and 2 display the measured values of M_A from neutrino and antineutrino experiments (this compilation is also presented in graphical form in Fig. 20). Whenever possible we provide also the M_A measured from the total cross section.

From the results described above one can conclude that the presently available experimental data on the neutrino QEL cross section allow for a very wide spread of the axial mass values, roughly from 0.7 to 1.3 GeV. Therefore the reliability of a theoretical fit to these data is questionable and the uncertainty attributed to such a fit should go beyond the averaged experimental statistical accuracy. Nevertheless, the formal averaging of M_A values from several early experiments was done by the authors of [33]: $M_A = 1.026 \pm 0.021$ GeV. This result is also known as the axial

Table 1 A summary of existing experimental data: the axial mass M_A as measured in previous neutrino experiments. Numbers of observed events have been taken from the original papers; usually they are not corrected for efficiency and purity (the so-called QEL candidates). The axial mass value for the NuTeV experiment [23] was estimated from the published neutrino quasi-elastic cross section ($\sigma_\nu^{qel} = (0.94 \pm 0.03(\text{stat}) \pm 0.07(\text{syst})) \times 10^{-38}$ cm^2); the systematic error for IHEP SKAT 90 [22] is 0.14 GeV

Experiment	Target	Events	Method	M_A, GeV	Ref.
ANL 69	Steel		$d\sigma/dQ^2$	1.05 ± 0.20	[1]
			σ	0.97 ± 0.16	
ANL 73	Deuterium	166	$d\sigma/dQ^2$	0.94 ± 0.18	[2]
			$\sigma \otimes d\sigma/dQ^2$	0.95 ± 0.12	
			σ	$0.75^{+0.13}_{-0.11}$	
ANL 77	Deuterium	~600	$d\sigma/dQ^2$	1.01 ± 0.09	[3]
			$\sigma \otimes d\sigma/dQ^2$	0.95 ± 0.09	
			σ	0.74 ± 0.12	
ANL 82	Deuterium	1737	$d\sigma/dQ^2$	1.05 ± 0.05	[4]
			$\sigma \otimes d\sigma/dQ^2$	1.03 ± 0.05	
BNL 81	Deuterium	1138	$d\sigma/dQ^2$	1.07 ± 0.06	[6]
BNL 90	Deuterium	2538	$d\sigma/dQ^2$	$1.070^{+0.040}_{-0.045}$	[8]
FermiLab 83	Deuterium	362	$d\sigma/dQ^2$	$1.05^{+0.12}_{-0.16}$	[9]
NuTeV 04	Steel	21614	σ	1.11 ± 0.08	[23]
MiniBooNE 07	Mineral oil	193709	$d\sigma/dQ^2$	1.23 ± 0.20	[26]
CERN HLBC 64	Freon	236	$d\sigma/dQ^2$	$1.00^{+0.35}_{-0.20}$	[11]
CERN HLBC 67	Freon	90	$\sigma \otimes d\sigma/dQ^2$	$0.75^{+0.24}_{-0.20}$	[12]
CERN SC 68	Steel	236	$d\sigma/dQ^2$	$0.65^{+0.45}_{-0.40}$	[13]
CERN HLBC 69	Propane	130	$\sigma \otimes d\sigma/dQ^2$	0.70 ± 0.20	[14]
CERN GGM 77	Freon	687	σ	0.88 ± 0.19	
			$d\sigma/dQ^2$	0.96 ± 0.16	[15]
CERN GGM 79	Propane/Freon	556	σ	0.87 ± 0.18	
			$d\sigma/dQ^2$	0.99 ± 0.12	[17]
CERN BEBC 90	Deuterium	552	σ	0.94 ± 0.07	
			$d\sigma/dQ^2$	1.08 ± 0.08	[18]
IHEP 82	Aluminium	898	$d\sigma/dQ^2$	1.00 ± 0.07	[19]
IHEP 85	Aluminium	1753	$d\sigma_{\nu+\bar{\nu}}/dQ^2$	1.00 ± 0.04	[20]
IHEP SCAT 88	Freon	464	$\sigma \otimes d\sigma/dQ^2$	0.96 ± 0.15	[21]
			σ	1.08 ± 0.07	
IHEP SCAT 90	Freon		$d\sigma/dQ^2$	1.05 ± 0.07	[22]
			$\sigma \otimes d\sigma/dQ^2$	1.06 ± 0.05	
K2K 06, SciFi	Water	~12000	$d\sigma/dQ^2$	1.20 ± 0.12	[24]
K2K 08, SciBar	Carbon		$d\sigma/dQ^2$	1.144 ± 0.077	[25]

mass world average value. According to [34–36] an updated world average value from ν_μ-deuterium and pion electroproduction experiments is $M_A = 1.014 \pm 0.014$ GeV.

3 The NOMAD detector

The NOMAD detector [29] consisted of an active target of 44 drift chambers with a total fiducial mass of 2.7 tons, located in a 0.4 Tesla dipole magnetic field as shown in Fig. 1.

The $X \times Y \times Z$ total volume of the drift chambers is about $300 \times 300 \times 400$ cm^3.

Drift chambers [37], made of low Z material served the dual role of a nearly isoscalar target[1] for neutrino interactions and of tracking medium. The average density of the

---

[1]The NOMAD active target is nearly isoscalar ($n_n : n_p = 47.56\% : 52.43\%$) and consists mainly of carbon; a detailed description of the drift chamber composition can be found in [37].

Table 2 The same as in Table 1, but for antineutrino experiments. The axial mass value for the NuTeV experiment [23] was estimated from the published antineutrino quasi-elastic cross section ($\sigma_{\bar{\nu}}^{qel} = (1.12 \pm 0.04(\text{stat}) \pm 0.10(\text{syst})) \times 10^{-38} \text{ cm}^2$); the systematic error for IHEP SKAT 90 [22] is 0.20 GeV

Experiment	Target	Events	Determined from	M_A, GeV	Ref.
BNL 80	Hydrogen		$d\sigma/dQ^2$	$0.9^{+0.4}_{-0.3}$	[5]
BNL 88	Liquid scint.	2919	$d\sigma/dQ^2$	1.09 ± 0.04	[7]
FermiLab 84	Neon	405	$d\sigma/dQ^2$	0.99 ± 0.11	[10]
NuTeV 04	Steel	15054	σ	1.29 ± 0.11	[23]
CERN GGM 77	Freon	476	σ	0.69 ± 0.44	[15]
			$d\sigma/dQ^2$	0.94 ± 0.17	
CERN GGM 79	Propane/Freon	766	σ	$0.84^{+0.08}_{-0.09}$	[16]
			$d\sigma/dQ^2$	0.91 ± 0.04	
IHEP 85	Aluminium	854	$d\sigma_{\nu+\bar{\nu}}/dQ^2$	1.00 ± 0.04	[20]
IHEP SKAT 88	Freon	52	$\sigma \otimes d\sigma/dQ^2$	0.72 ± 0.23	[21]
			σ	0.62 ± 0.16	
IHEP SKAT 90	Freon		$d\sigma/dQ^2$	0.79 ± 0.11	[22]
			$\sigma \otimes d\sigma/dQ^2$	0.71 ± 0.10	

Fig. 1 A side-view of the NOMAD detector
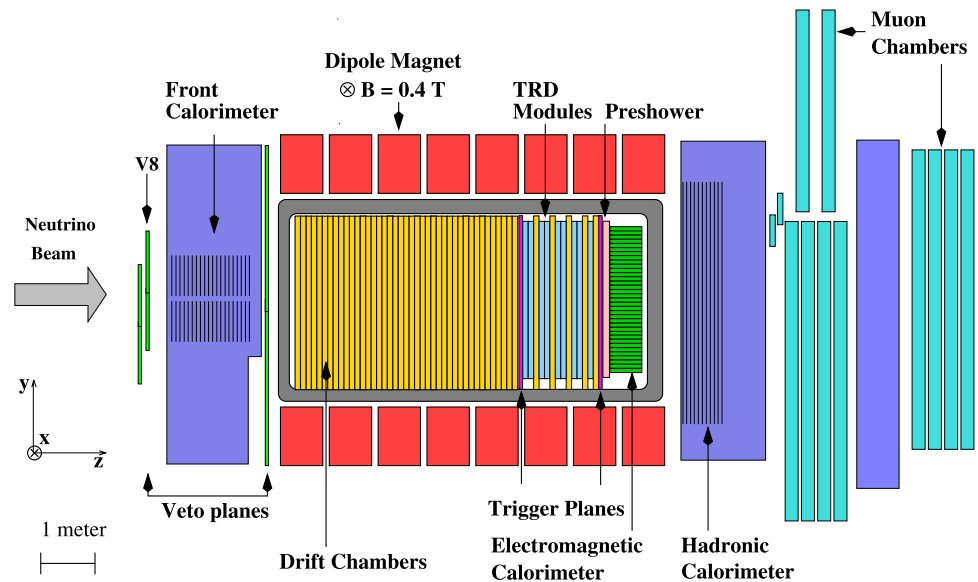
drift chamber volume was 0.1 g/cm^3. These chambers provided an overall efficiency for charged track reconstruction of better than 95% and a momentum resolution which can be approximated by the following formula $\frac{\sigma_p}{p} \approx \frac{0.05}{\sqrt{L}} \oplus \frac{0.008p}{\sqrt{L^5}}$, where the momentum p is in GeV/c and the track length L in m. Reconstructed tracks were used to determine the event topology (the assignment of tracks to vertices), to reconstruct the vertex position and the track parameters at each vertex and, finally, to identify the vertex type (primary, secondary, etc.). A transition radiation detector (TRD) [38, 39] placed at the end of the active target was used for particle identification. Two scintillation counter trigger planes [40] were used to trigger on neutrino interactions in the NOMAD active target. A lead-glass electromagnetic calorimeter [41,

42] located downstream of the tracking region provided an energy resolution of $3.2\%/\sqrt{E[\text{GeV}]} \oplus 1\%$ for electromagnetic showers and was crucial to measure the total energy flow in neutrino interactions. In addition, an iron absorber and a set of muon chambers located after the electromagnetic calorimeter was used for muon identification, providing a muon detection efficiency of 97% for momenta greater than 5 GeV/c.

The NOMAD neutrino beam consisted mainly of ν_μ's with an about 7% admixture of $\bar{\nu}_\mu$ and less than 1% of ν_e and $\bar{\nu}_e$. More details on the beam composition can be found in [30].

The main goal of the NOMAD experiment was the search for neutrino oscillations in a wide-band neutrino beam from

the CERN SPS [43, 44]. A very good quality of event reconstruction similar to that of bubble chamber experiments and a large data sample collected during four years of data taking (1995–1998) allow for detailed studies of neutrino interactions.

3.1 Reconstruction of QEL events in the NOMAD detector

A detailed information about the construction and performance of the NOMAD drift chambers as well as about the developed reconstruction algorithms is presented in [37]. Let us briefly describe some features relevant to the current QEL analysis. The muon track is in general easily reconstructed. However, when we study protons emitted in the ν_μ QEL two-track candidates we deal with protons with momentum well below 1 GeV/c and with emission angle above 60 degrees. For positive particles in the upward hemisphere of the NOMAD detector such conditions mean that these particles are almost immediately making a U-turn due to the magnetic field. There were no special efforts invested into tuning the NOMAD reconstruction program to reconstruct this particular configuration (which is rather difficult due to the fact that these protons are in the $1/\beta^2$ region of ionization losses, traversing much larger amount of material, crossing drift cells at very large angles where the spacial resolution of the drift chambers is considerably worse and where a large amount of multiple hits is produced, etc.). Some of these effects are difficult to parameterize and to simulate at the level of the detector response in the MC simulation program. Thus, the reconstruction efficiencies for this particular configuration of outgoing protons could be different for the simulated events and real data.

Let us stress, however, that for protons emitted downwards we observed a good agreement between data and MC (see Fig. 6 below).

In the current analysis it was important to disentangle the reconstruction efficiency effects discussed above from the effects induced by intranuclear cascade (which could change the proton kinematics and thus introduce drastic changes in the final results due to the efficiency mismatch between simulated and real data). In order to get rid of an interplay between these two effects it was crucial to choose the region in the detector with a stable reconstruction efficiency. This could be achieved by selecting ν_μ QEL events where protons are emitted in the lower hemisphere of the NOMAD detector. Therefore during the event selection we apply a cut on the muon to be emitted in the upper hemisphere (see Sect. 5).

The most upstream drift chamber was used as an additional veto to remove through-going muons from neutrino interactions upstream of the NOMAD active target. This is crucial for the study of single track events.

4 Monte Carlo simulation of neutrino interactions and analysis procedure

Inclusive (anti)neutrino charged-current (CC) and neutral current (NC) scattering can be considered as a mixture of several processes described by significantly different models. In our case, these are quasi-elastic scattering (QEL), single-pion production via intermediate resonance state (RES) and deep inelastic scattering (DIS). There is also a contribution from a coherent interaction of neutrino with a nucleus as a whole (COH). Below we will describe in details the simulation scheme used for each of these processes and discuss the influence of the nuclear effects.

The overall procedure used to compute the QEL cross section and extract M_A is as follows. Analytical expressions described in Sect. 4.6 are used to compute the numbers of produced background events. A Monte Carlo program, described below, is used to calculate the efficiencies for the various background sources to survive the selection procedure described in Sect. 5. These efficiencies are then applied to the numbers of produced events to calculate the background in our final sample and subtract it, yielding the numbers of QEL events. The QEL cross sections are extracted from them after correcting for the QEL efficiency. As a last step, the analytical expression for the QEL cross section is used to find the value of M_A that best fits our results.

4.1 Quasi-elastic neutrino scattering

The standard representation of the weak hadronic current involved in the matrix elements of the processes $\nu_\mu n \to \mu^- p$ and $\bar{\nu}_\mu p \to \mu^+ n$, is expressed in terms of 6 form factors, which in general are assumed to be complex [45]. They formally describe the hadronic structure and cannot be calculated analytically within the framework of the electro-weak interaction theory.

We neglect the second-class current contributions associated with the scalar and pseudo-tensor form factors. This is equivalent to the requirement of time reversal invariance of the matrix element (hence all form factors should be real functions of Q^2) and charge symmetry of the hadronic current (rotation about the second axis in the isotopic space).

The vector form factors F_V and F_M are related through the isospin symmetry hypothesis to the electromagnetic ones, which we will consider to be well known. Instead of the simple dipole parameterization, extensively used in previous experiments, we have chosen the Gari–Krüempelmann (GK) model [46] extended and fine-tuned by Lomon [47]. Specifically we explore the "GKex(05)" set of parameters [48] which fits the modern and consistent older data well and meets the requirements of dispersion relations and of QCD at low and high 4-momentum transfer [46].

For the axial and pseudo-scalar form factors we use the conventional representations [45]:

$$F_A(Q^2) = F_A(0)\left(1 + \frac{Q^2}{M_A^2}\right)^{-2} \tag{1}$$

and

$$F_P(Q^2) = \frac{2m_N^2}{m_\pi^2 + Q^2} F_A(Q^2), \tag{2}$$

where $F_A(0) = g_A = -1.2695 \pm 0.0029$ (measured in neutron β-decay [49]); m_π and m_N are the pion and nucleon masses.

As discussed in Sect. 2, the currently available experimental data on the axial mass M_A allow for a wide spread. Thus, in our case, it should be considered as one of the available parameters, which can be used to adjust the MC simulation with the measured value of the total QEL cross section and observed distributions of the kinematic variables (other parameters, related to the modeling of the intranuclear cascade, will be described later).

Note that the expression for the pseudo-scalar form factor F_P is nothing better than a plausible parameterization inspired by the PCAC hypothesis and the assumption that the pion pole dominates at $Q^2 \lesssim m_\pi^2$ [45]. However, its contribution enters into the cross sections multiplied by a factor $(m_\mu/m_N)^2$. Hence, the importance of the related uncertainty is much reduced.

4.2 Single-pion production through intermediate baryon resonances

In order to describe the single-pion neutrino production through baryon resonances we adopt an extended version of the Rein and Sehgal model (RS) [50, 51], which seems to be one of the most widely trusted phenomenological approaches for calculating the RES cross sections. The generalization proposed in [52, 53] takes into account the final lepton mass and is based upon a covariant form of the charged leptonic current with definite lepton helicity. In our MC simulation we use the same set of 18 interfering nucleon resonances with masses below 2 GeV as in [50] but with all relevant input parameters updated according to the current data [49, 54]. Significant factors (normalization coefficients etc.), estimated in [50] numerically are recalculated by using the new data and a more accurate integration algorithm.

The relativistic quark model of Feynman, Kislinger, and Ravndal [55], adopted in the RS approach, unambiguously determines the structure of the transition amplitudes involved into the calculation and the only unknown structures are the vector and axial-vector transition form factors $G^{V,A}(Q^2)$. In [50] they are assumed to have the form

$$\frac{G^{V,A}(Q^2)}{G^{V,A}(0)} = \left(1 + \frac{Q^2}{4m_N^2}\right)^{1/2-n} \left(1 + \frac{Q^2}{M_{V,A}^2}\right)^{-2}, \tag{3}$$

where the integer n in the first ("ad hoc") factor in (3) is the number of oscillation quanta of the intermediate resonance.

The vector mass M_V is taken to be 0.84 GeV, that is the same as in the usual dipole parameterization of the nucleon electromagnetic form factors. The axial mass (which was fixed at 0.95 GeV in the original RS paper) is set to the standard world averaged value $M_A = 1.03$ GeV. It is in good agreement with the results obtained in the recent analysis of the data from the BNL 7-foot deuterium filled bubble chamber: $M_A = 1.08 \pm 0.07$ GeV [56]. Let us also note that the available experimental data for the single-pion neutrino production (as in the case of QEL scattering) does not permit a very definite conclusion about the value of the total RES cross section (and the corresponding axial mass value). The present uncertainties will be taken into account in the calculation of the systematic error of the current analysis.

To compensate for the difference between the SU_6 predicted value ($-5/3$) and the experimental value for the nucleon axial-vector coupling g_A, Rein and Sehgal introduced a renormalization factor $Z = 0.75$. In order to adjust the renormalization to the current world averaged value $g_A = -1.2695$ [49] we have adopted $Z = 0.762$. The harmonic-oscillator constant Ω, which accounts for the mass differences between states with different number of excitation quanta is set to its original value $\Omega = 1.05$ GeV^2.

Another essential ingredient of the RS approach is the non-resonant background (NRB). Its contribution is important in describing the existing data on the reactions $\nu_\mu n \rightarrow \mu^- n\pi^+$, $\nu_\mu n \rightarrow \mu^- p\pi^0$, $\bar{\nu}_\mu p \rightarrow \mu^+ p\pi^-$ and $\bar{\nu}_\mu p \rightarrow \mu^+ n\pi^0$. In our Monte Carlo, the NRB is taken to come from the DIS part of the simulation. Therefore it has not been used in the RES part of our event generator.

4.3 Deep inelastic scattering

The MC simulation of the deep inelastic neutrino–nucleon scattering is based on the LEPTO 6.5.1 package [57] with several modifications [58, 59]. For hadronization we use the LUND string fragmentation model, as incorporated into the JETSET 7.4 program [60–62]. Structure functions are calculated at LO using the GRV98 [63] parton distribution functions.

Upon implementing the Monte Carlo for ν_μ ($\bar{\nu}_\mu$) CC scattering, kinematic boundaries between exclusive (RES) and inclusive (DIS) channels must be defined. To avoid double counting, the phase space of the RES and DIS contributions should be separated by the conditions $W < W_{\text{cut}}^{\text{RES}}$ and $W > W_{\text{cut}}^{\text{DIS}}$, where W is the invariant mass of the final hadronic system.

The maximum possible value for $W_{\text{cut}}^{\text{RES}}$ is the upper limit of the RS model (2 GeV), while inelastic scattering can take place from the one-pion production threshold (note, however, that this value is too small in principle since the struc-

ture functions used in the calculation of the DIS cross section cannot be extrapolated down to this value).

Unfortunately, there is no clear physical recipe to determine exact numerical values for those cutoff parameters. The authors of GENIE MC code [64] adopt the value $W_{cut}^{RES} \simeq W_{cut}^{DIS} \sim 1.7$ GeV. A comprehensive analysis of available experimental data made in [65, 66] suggests to decrease this cut to ~ 1.5 GeV.

In the present analysis we set $W_{cut}^{RES} = 2$ GeV and $W_{cut}^{DIS} = 1.4$ GeV. This choice allows for the non-resonant contribution to single-pion production to be accounted for by the DIS part of the Monte Carlo, providing e.g. $N(\mu^- p \pi^0$ in DIS$)/N_{dis} \cdot \sigma_{dis} \approx \sigma(\mu^- p \pi^0$ in NRB from RES), see previous subsection. Moreover, it is not at variance with experimental data as far as the total (anti)neutrino cross section is concerned.

4.4 Coherent pion production

In the processes described above, neutrinos interact with individual target nucleons. However, pions can be produced in a coherent interaction of the neutrino with the whole nucleus, i.e. in the case of CC ν_μ scattering $\nu_\mu \mathcal{N} \rightarrow \mu^- \pi^+ \mathcal{N}$, where $\mathcal{N}$ is the target nucleus.

The details of the MC simulation can be found in [67], which is devoted to the investigation of this process in the NOMAD experiment. The flux-averaged cross section has been calculated following [68, 69] and has been estimated at 0.733×10^{-38} cm^2 per nucleus. For a recent experimental result at low incoming neutrino energy see [70]. Taking into account that the average mass number of the NOMAD target is 12.9, and using the number of recorded DIS events (see Sect. 6.1.1) one finds that the expected number of coherent pion production events is ~ 2700. Nevertheless, the probability for events of this type to be identified as QEL is $\sim 2\%$ because of the small pion emission angle, so that the expected contamination of the selected QEL sample is lower than 0.4%.

4.5 Nuclear effects

For typical NOMAD neutrino energies, we can assume that the incident neutrino interacts with one nucleon only inside the target nucleus, while the remaining nucleons are spectators (Impulse Approximation). In this case, one can describe the neutrino nucleus scattering by folding the usual expressions for the free neutrino–nucleon cross sections with a Fermi gas distribution.

In the relativistic Fermi gas model, the nucleus is considered as an infinite system of non-interacting nucleons. The phenomena related to the nuclear surface and to the interaction between nucleons can be taken into account by using a
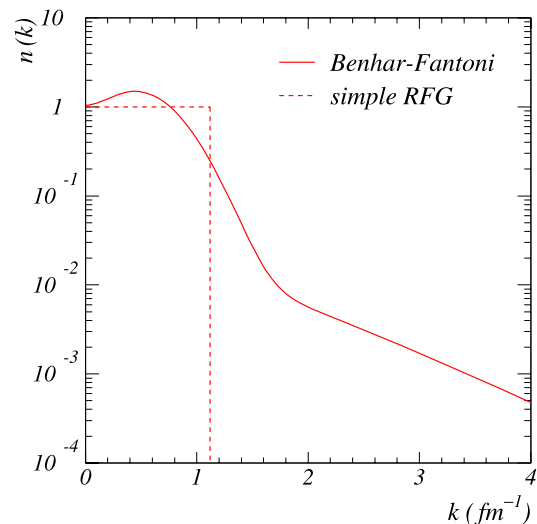
Fig. 2 Benhar–Fantoni parameterization [71] for the momentum distribution of the target nucleons (*solid line*), normalized to the Fermi distribution with zero temperature and Fermi momentum $P_F = 221$ MeV/c (simple RFG, *dashed line*)

more realistic effective momentum distribution for the target nucleons. In the NOMAD event generator we used the Benhar–Fantoni parameterization [71], see Fig. 2.

The QEL simulation is based on the Smith-Moniz approach [72]. The momentum of the recoil nucleus and the nucleon binding energy are included in the conservation laws which determine the event kinematics. The only final state interaction (FSI) effect which is taken into account at this stage is the Pauli exclusion principle. The explicit form of the QEL differential cross section used in the MC code can be found in [32].

MC implementation of the Fermi gas model in the case of single-pion production is more straightforward. First, we generate the momentum of the target nucleon and make a Lorentz boost to its rest frame where the RES event can be simulated according to the extended RS model described in Sect. 4.2. The effect of Pauli blocking on the outgoing nucleon is taken into account as it is in the QEL MC.

In the case of the DIS neutrino scattering there are several specific nuclear effects (such as nuclear shadowing, pion excess and off-shell corrections to bound nucleon structure functions). They are described in the theoretical framework proposed in [73].

Simulating the re-interactions between particles produced at the primary neutrino collision off the target nucleon with the residual nucleus is an important ingredient of the MC event generator. To include this effect, commonly called final state interactions, we use the DPMJET package [74].

The intranuclear re-interaction of the particles generated by the QEL, RES or DIS event generators can be described and simulated by the Formation Zone Intranuclear Cascade model [75, 76] implemented in DPMJET. Secondaries from

the first collision are followed along straight trajectories and may induce in turn intranuclear cascade processes if they reach the end of their "formation zone" inside the target; otherwise they leave the nucleus without interacting.

There are two important parameters in DPMJET. The first one, called the formation time τ_0, controls the development of the intranuclear cascade. With increasing τ_0, the number of cascade generations and the number of low-energy particles will be reduced. Its default value is $\tau_0 = 2.0$. After some tuning described below we adopted the value $\tau_0 = 1.0$ in our simulation of QEL and RES events.

Inside DPMJET, the momenta of the spectator nucleons are sampled from the zero temperature Fermi distribution. However, the nuclear surface effects and the interaction between nucleons result in a reduction of the Fermi momentum, see Fig. 2. It can be accounted for by introducing a correction factor α_{mod}^F (default value 0.6). Moreover, α_{mod}^F provides the possibility of some modification of the momentum distribution for the emitted low-energy nucleons.

At the end of the intranuclear cascade, the residual nucleus is supposed to go through some de-excitation mechanisms. It can be disrupted into two or more fragments, emit photons, nucleons or light particles (like d, α, ^{3}H, ^{3}He). We can easily neglect this contribution, since the typical energy of those particles is below the observation threshold of the NOMAD detector.

In our analysis, special attention will be devoted to the dependence of the obtained results on the intranuclear cascade parameters. As a cross-check, we compare our MC simulation for the QEL process with the predictions of the NUANCE event generator [77], which is currently used in a large number of neutrino experiments and which contains a different approach to the modeling of FSI effects.

4.6 Analytical models used to fit the data

In this subsection we estimate the number of signal quasi-elastic events in the initial ν_μ ($\bar{\nu}_\mu$) CC sample.

The contribution of each process to the total set of events is proportional to its flux-averaged cross section:

$$\langle\sigma\rangle = \int \sigma(E_\nu)\Phi(E_\nu)dE_\nu \Big/ \int \Phi(E_\nu)dE_\nu, \tag{4}$$

where

$$\sigma(E_\nu) = n_n\sigma_{\nu n}(E_\nu) + n_p\sigma_{\nu p}(E_\nu)$$

is the theoretical prediction for the cross section of the process at stake, $\Phi(E_\nu)$ denotes the NOMAD (anti)neutrino energy spectrum[2] (see Fig. 3); n_n (n_p) is the relative fraction of neutrons (protons) in the NOMAD target (see Sect. 3).
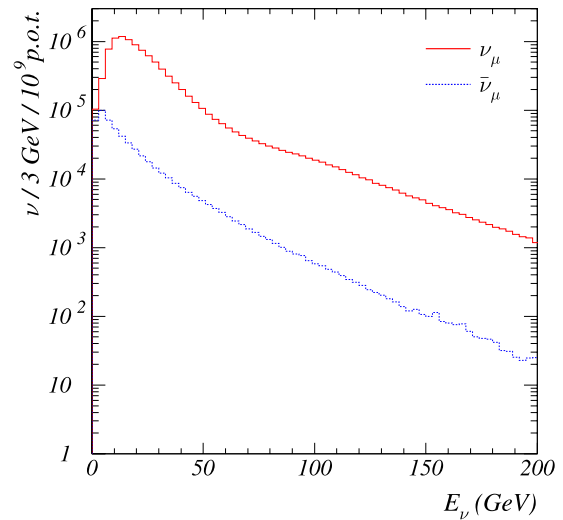
Fig. 3 The predicted energy spectra of ν_μ and $\bar{\nu}_\mu$ at NOMAD for the transverse fiducial area of 100×100 cm^2
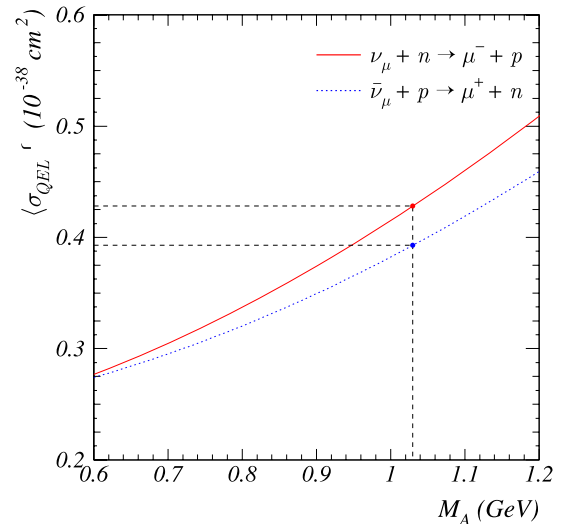

Fig. 4 Flux-averaged cross section of QEL (anti)neutrino scattering for the NOMAD ν_μ($\bar{\nu}_\mu$) beam as a function of the axial mass M_A

The QEL cross section was calculated in the framework of the Smith and Moniz model [72] for carbon with binding energy $E_b = 25.6$ MeV and Fermi momentum $P_F = 221$ MeV/c. No final state interactions are taken into account apart from Pauli blocking. As noted above, the final result depends strongly on the axial mass M_A (see Fig. 4).

To estimate the RES contribution, we fold the extended RS model [53] for a free nucleon with the Pauli factor from [79]. The computation of $\sigma_{dis}(E_\nu)$ has been done with the GRV98-LO PDF model as indicated in [65]. The cut-off parameters W_{cut}^{RES} and W_{cut}^{DIS} are the same as for the MC simulation. The analytical calculations do not include nu-
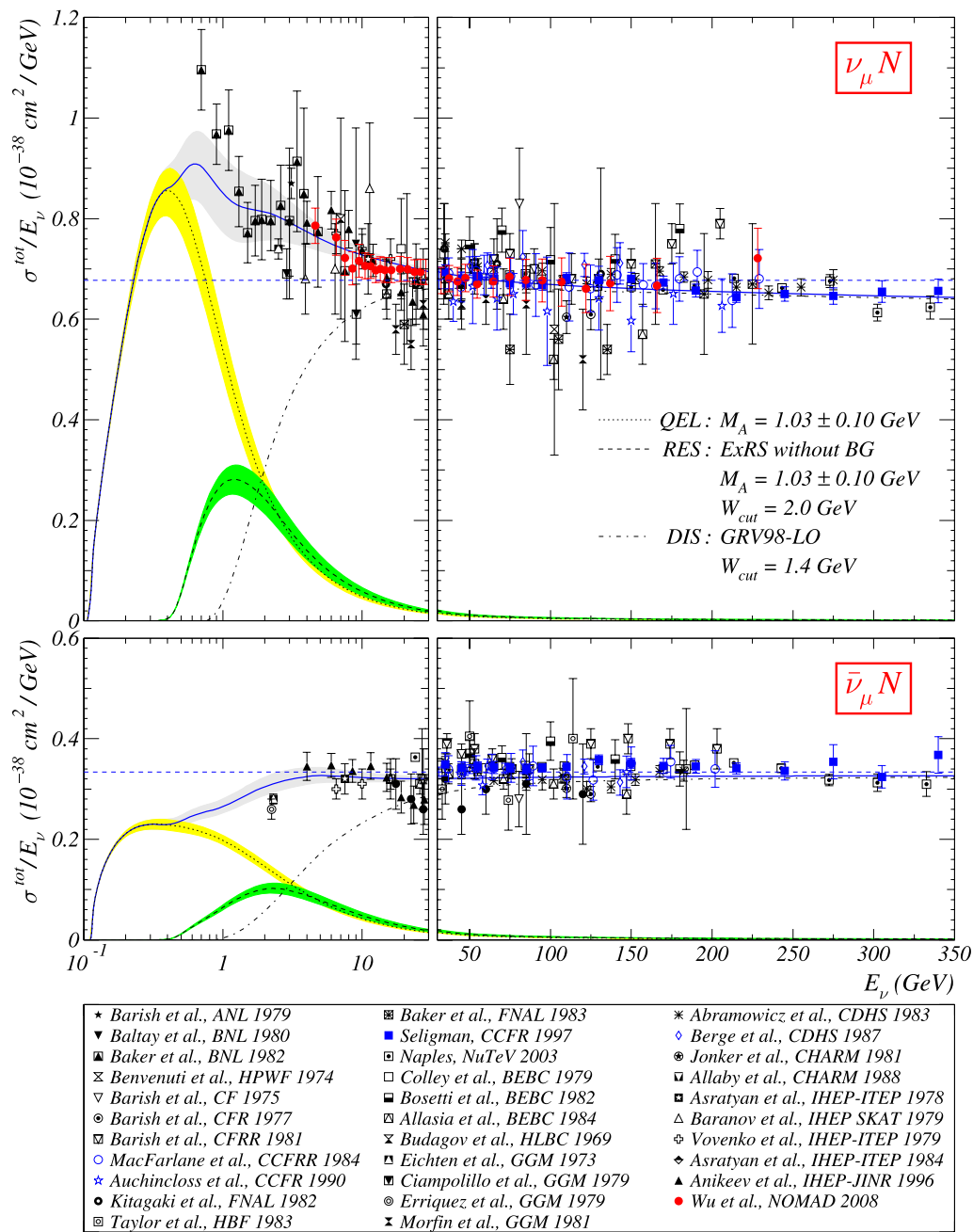
Fig. 5 Slopes of the total ν_μ and $\bar{\nu}_\mu$ CC scattering cross sections off an isoscalar nucleon. Experimental data come from [65] and from [78] for the NOMAD points. The smooth curves show the QEL, RES, and DIS contributions and their sums calculated as described in Sect. 4.6. RES and DIS are used in this analysis to subtract background from experimental data (see (11)). The axial mass M_A, which enters both QEL and RES, is given the value used in our Monte-Carlo. The bands reflect a $\pm 10\%$ variation around it, roughly spanning the core of the hitherto published measurements. Our final result for M_A is 2–3% above the MC value (see (25)–(27)). Also shown are the energy averaged slopes published by the Particle Data Group [49]: $(0.677 \pm 0.014) \times 10^{-38}$ cm^2/GeV for $\nu_\mu N$ and $(0.334 \pm 0.008) \times 10^{-38}$ cm^2/GeV for $\bar{\nu}_\mu N$

clear corrections and final state interactions apart from Pauli blocking.

The results from these calculations are shown as curves in Fig. 5 which also includes a compendium of total (anti)-neutrino cross-section data.

Table 3 contains our results for the reduced fiducial volume of the NOMAD detector: $|X, Y| \leqslant 100$ cm; the average ν_μ ($\bar{\nu}_\mu$) energy was 25.9 (17.6) GeV.

Combining all these, the expected fraction of quasi-elastic events in the initial ν_μ ($\bar{\nu}_\mu$) CC sample before any

Table 3 Flux-averaged cross sections of the QEL, RES, DIS CC and NC processes per one nucleon of the NOMAD target. Neutrino beam spectrum corresponds to the $|X, Y| \leqslant 100$ cm fiducial area. The unit used for the cross section is 10^{-38} cm^2

Process type	ν_μ	$\bar{\nu}_\mu$
QEL	0.428	0.393
RES	0.576	0.432
DIS CC	16.643	4.876
DIS NC	5.335	

special selection is about 2.4% (6.9%) or $\sim$20300 ($\sim$1360) events.

5 Events selection

In this section we describe particular features of reconstruction and identification of ν_μ and $\bar{\nu}_\mu$ QEL events.

5.1 $\nu_\mu n \to \mu^- p$ selection

For a $\nu_\mu n \to \mu^- p$ event one can expect two tracks originating from the reconstructed primary vertex:[3] one of them should be identified as a muon, while the second track is assumed to be a proton. Later we shall refer to events with such a topology as 2-track events.[4]

Sometimes the proton track cannot be reconstructed, e.g. if its momentum is below the detector registration threshold. In this case, we deal with only one muon track and we call such an event a 1-track event.

The expected ratio between 1-track and 2-track events for the pure standard QEL MC sample is 54.3% : 45.7%.

There are three possible reasons for the reconstruction of the proton track in a QEL event to fail:

– the proton, which was born in the neutrino interaction with the target nucleon, has too low a momentum or too large an emission angle (this depends on the parameters of the model used to describe the neutrino–nucleon interaction, in particular, on the value of the axial mass);

– the proton from the primary neutrino interaction was involved in an intranuclear cascade and lost part of its energy (this is controlled by the DPMJET parameters, mainly by the formation time τ_0);

---

[3]All charged tracks originating within a 5 cm box around the reconstructed primary vertex are forced to be included into it; we have also tried to vary this parameter by enlarging the size of the box to 10 cm and found that the final results are rather stable (within 0.3% for the measured QEL cross section).

[4]In this analysis we do not take into account clusters in the electromagnetic calorimeter, which can be associated with neutral particles, originating from the primary vertex.

– the detector magnetic field deviates positively charged particles upwards; therefore, if a slow proton is emitted at an azimuth $\varphi_h \sim \pi/2$, its trajectory is almost parallel to the drift chamber planes and its track reconstruction efficiency (which depends on the number of hits associated with the track) is significantly lower than in the case of a proton emitted downwards at $\varphi_h \sim 3\pi/2$.

In Fig. 6 (left) we illustrate these last two effects: the magnetic field is the cause of the asymmetry in the azimutal distribution of the reconstructed protons, while varying the formation time parameter τ_0 affects the expected number of tracks uniformly.

In Fig. 7 we display an example of distributions of the leading proton momentum p_h and emission angle θ_h before and after FSI for the QEL neutrino scattering. The proton reconstruction probabilities are also shown as functions of p_h and θ_h: one can observe a fast decrease at low proton momenta (below 300 MeV/c) and large emission angles (larger than 72°). So, FSI tends to increase the fraction of events in kinematic domains with low proton reconstruction efficiency and therefore to change the expected fraction of events with a given topology in the identified QEL sample.

Using 2-track events only for the analysis may seem very attractive, since we could significantly reduce the background contamination with the help of additional kinematic variables (details can be found below). However, the results thus obtained might still have large systematic uncertainties coming from insufficient understanding of nuclear effects.

The QEL events which are not reconstructed as 2-track events will populate mainly the 1-track sample. But σ_{qel} extracted from this sample will suffer from the same source of uncertainty. However, the measurement of the QEL cross section simultaneously from both samples is expected to have only little dependence on the uncertainties in the modeling of FSI effects and this is indeed what is found in the data (see Sect. 8).

Therefore, the strategy of our analysis (selection criteria) in the case of $\nu_\mu n \to \mu^- p$ can be outlined as follows.

– *Fiducial volume cut.* The reconstructed primary vertex should be within the restricted[5] fiducial volume (FV):

$$|X, Y| \leqslant 100 \text{ cm}, \qquad 25 \leqslant Z \leqslant 395 \text{ cm} \qquad (5)$$

– *Identified muon.* We require the presence of a reconstructed and identified negatively or positively charged muon for the neutrino and antineutrino analyses respectively. In order to avoid possible problems with detector reconstruction inefficiencies (see discussion in Sect. 3.1), we require $0 < \varphi_\mu < \pi$, where φ_μ is the muon azimuthal

---

[5]We use a more stringent cut $Z > 50$ cm for the data collected during 97 and 98, when the first drift chamber module was substituted by the NOMAD STAR detector.
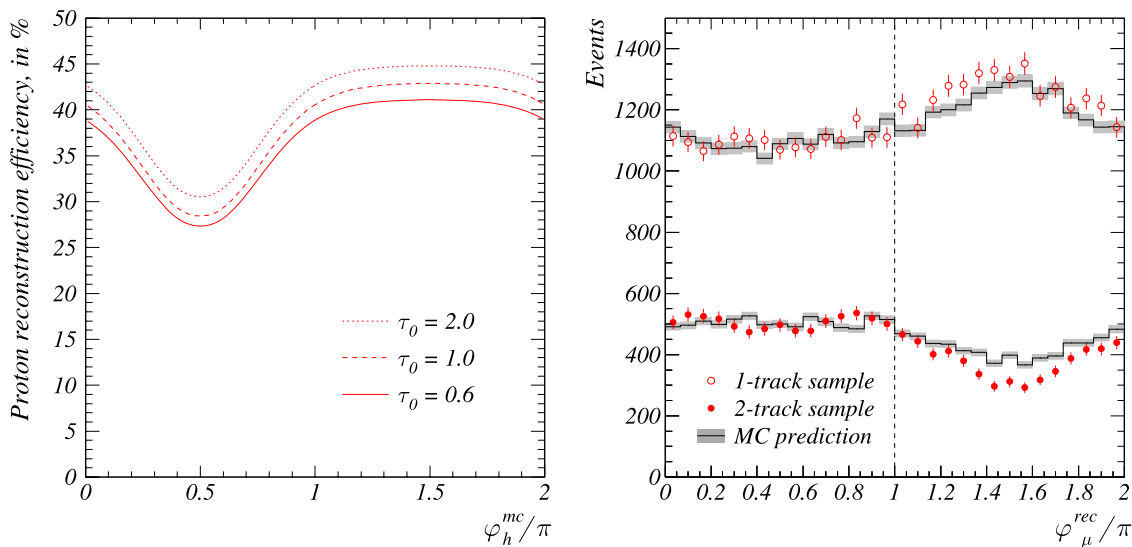
Fig. 6 Reconstruction efficiency of the proton track as a function of its azimuth φ_h for ν_μ QEL scattering; the curves are smoothed MC predictions obtained for different values of the formation time τ_0 (*left*). Comparison of the muon azimuth φ_μ distributions in data and MC for 1-track and 2-track samples (*right*); the *vertical dashed line* corresponds to the cut $0 < \varphi_\mu < \pi$ which was applied during the event selection
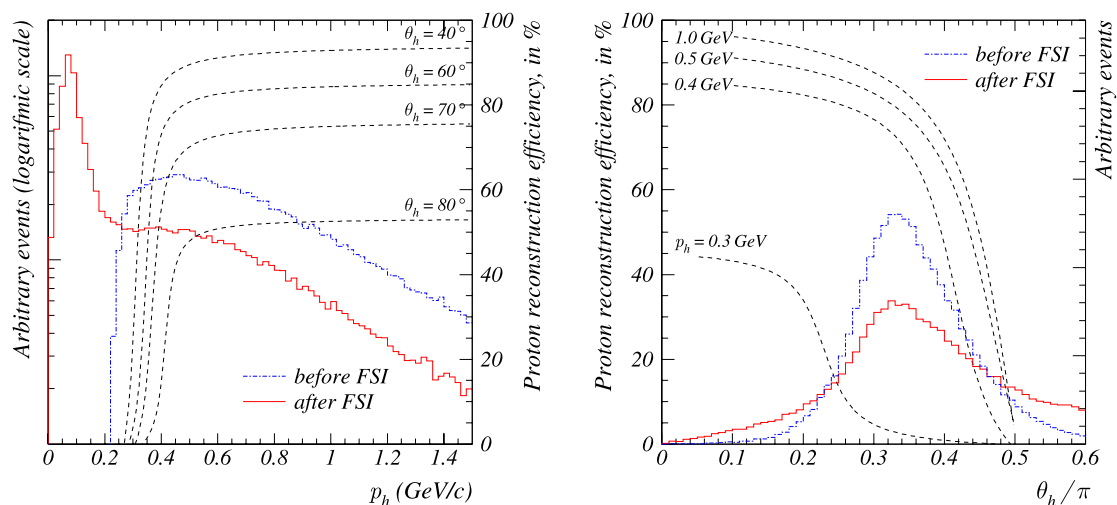
Fig. 7 Distribution of the leading proton momentum (*left*) and emission angle (*right*) before (*dash-dotted line*) and after (*solid line*) FSI simulation. *Dashed lines* show the proton reconstruction efficiency as a function of the proton momentum and emission angle (for $\pi < \varphi_h < 2\pi$)

angle (so, the proton track should lie in the bottom hemisphere), see Fig. 6 (right).

This choice is validated by our final errors being dominated by systematics as will be shown below.

– *Event topology and reconstructed kinematic variables.* We assign the events to the 1-track and 2-track subsamples and calculate E_ν and Q^2.

– *Single track sample* (only one charged lepton is reconstructed and identified). To avoid contamination from the through-going muons we extrapolate the muon track to the first drift chamber and require the absence

of veto chamber hits in the vicinity of the intersection point. The effectiveness of this quality cut was controlled by visual scanning of the reconstructed 1-track events in the experimental data. Another quality cut was used to suppress a possible contribution from inverse muon decay events: we require the muon transverse momentum to be greater than 0.2 GeV/c (see Sect. 6.1 for more details).

The kinematic variables are reconstructed under the assumption that the target nucleon is at rest. For the 1-track events, the muon momentum and direction are the sole measurements and we have to use the conser-

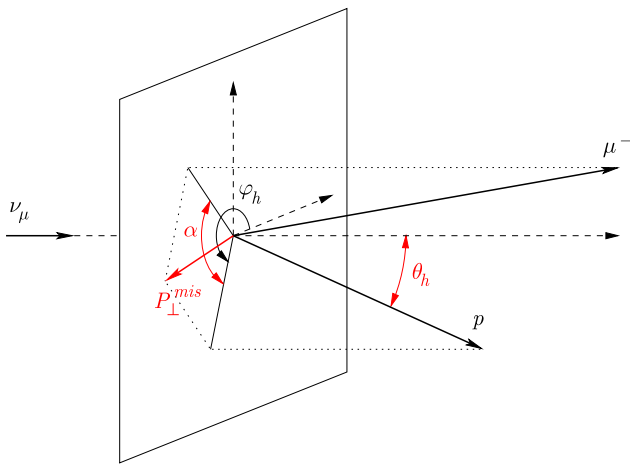vation laws (assuming QEL) to compute other kinematic quantities:

$$E_\nu = \frac{M E_\mu - m_\mu^2/2}{M - E_\mu + p_\mu \cos\theta_\mu},$$

$$Q^2 = 2M(E_\nu - E_\mu), \tag{6}$$

$$p_h = \left((E_\nu - p_\mu \cos\theta_\mu)^2 + p_\mu^2 \sin^2\theta_\mu\right)^{1/2},$$

$$\cos\theta_h = (E_\nu - p_\mu \cos\theta_\mu)/p_h,$$

where p_μ, θ_μ (p_h, θ_h) are the momentum and emission angle of the outgoing muon (nucleon); see Fig. 8. We note that for the neutrino energies relevant for this analysis (above 3 GeV) there is no difference between

Fig. 8 Likelihood variables: missing transverse momentum $P_\perp^{\mathrm{mis}}$, proton emission angle θ_h, angle α between the transverse components of the charged tracks

the calculations based on the approximated formulae above and the precise one, which takes into account the binding energy (see e.g. (4) in [26]). With the help of the MC simulation we estimate the resolution of the reconstructed E_ν and Q^2 as 3.6% and 7.8% respectively.

– *Two track sample* (both the negative muon and the positively charged track are reconstructed). For a reliable reconstruction, we require that the number of hits associated with the positively charged track should be greater than 7 and its momentum $p_h > 300$ MeV/c. Otherwise such an event is downgraded to the 1-track sample.

For 2-track events, we use both the muon and the proton reconstructed momenta to estimate E_ν and Q^2:

$$E_\nu = p_\mu \cos\theta_\mu + p_h \cos\theta_h,$$

$$Q^2 = 2E_\nu(E_\mu - p_\mu \cos\theta_\mu) - m_\mu^2.$$

The expected resolutions for E_ν and Q^2 are 3.6% and 7.1%.

The quality of the neutrino energy E_ν reconstruction for 1- and 2-track samples is illustrated in Fig. 9. It was checked that for the 2-track sample the derived cross sections are consistent within errors for both methods of E_ν calculation.

– *Background suppression*. The contamination from RES and DIS processes can be suppressed by using the difference between kinematical distributions in the QEL and background events as well as by the identification of the reconstructed positively charged track as a proton (for the 2-track sample only). Therefore we apply the following.

– *Identification of the positively charged track.*

The momentum-range method [80] can be reliably applied for low energy protons since their tracks are
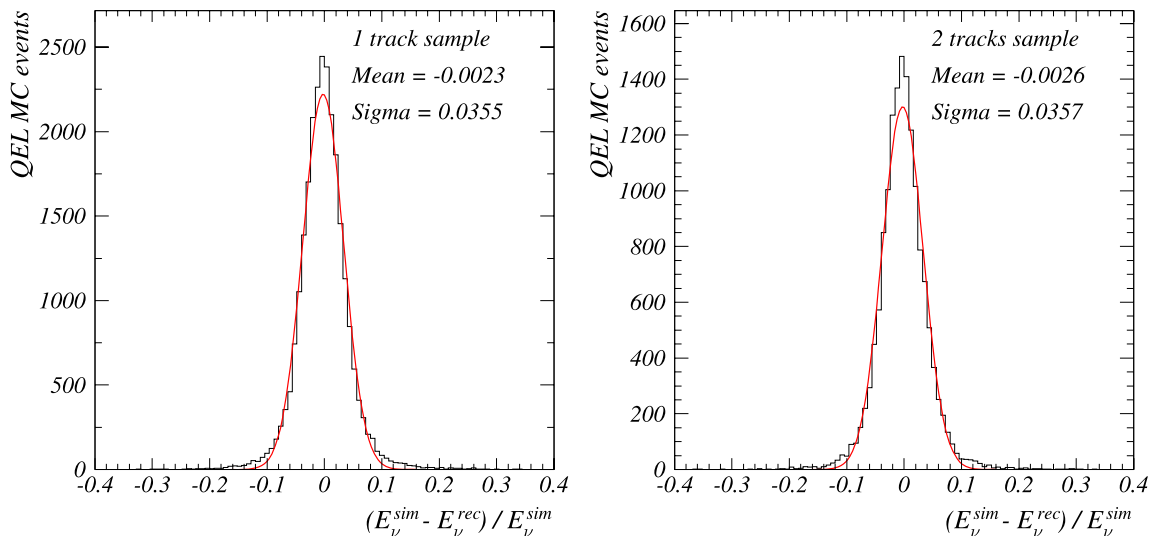
Fig. 9 The quality of the neutrino energy E_ν reconstruction for 1- and 2-track samples
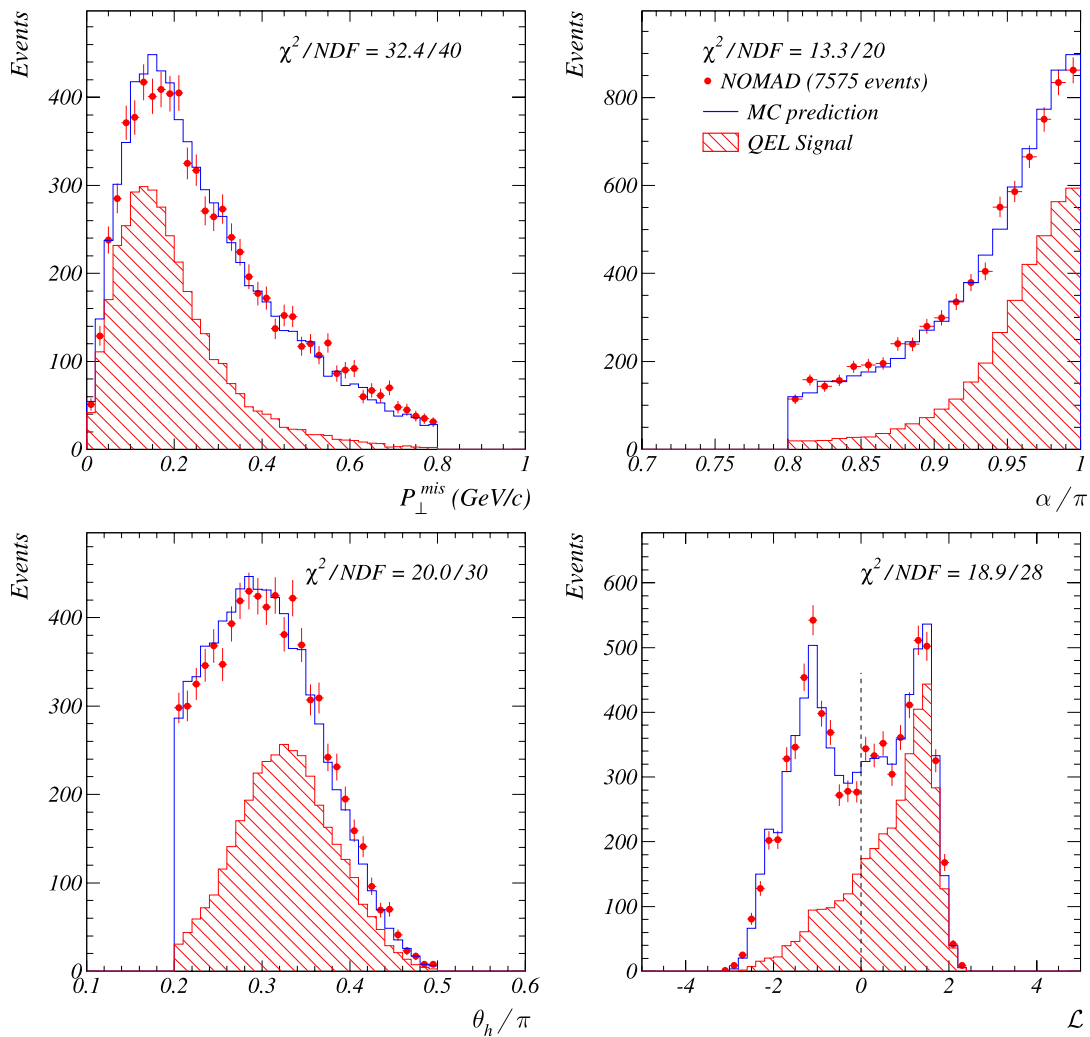
Fig. 10 The $P_\perp^{\mathrm{mis}}$, α, θ_h and likelihood distributions for a mixture of QEL, RES and DIS simulated events (histograms) compared to real data (points with error bars). The MC distributions are normalized to the number of events observed in the data

shorter compared to that of π^+ (the main background for proton identification) due to larger ionization losses. In our case, this method can be applied to about 17% of the events.[6]

– *Kinematical criteria.*

In the case of the 2-track sample, we can use additional kinematic variables to suppress background con-

tamination. We build the likelihood ratio

$$\mathcal{L} = \ln \frac{P(\ell\,|\mathrm{QEL})}{P(\ell\,|\mathrm{BG})}, \qquad (7)$$

using 3-dimensional correlations between the following kinematic variables (see Fig. 8): the missing transverse momentum $P_\perp^{\mathrm{mis}}$, the proton emission angle θ_h, and the angle α between the transverse components of the charged primary tracks. The following precuts were applied prior to the likelihood construction: $P_\perp^{\mathrm{mis}} < 0.8\,\mathrm{GeV}/c$, $0.2 \leqslant \theta_h/\pi \leqslant 0.5$ and $\alpha/\pi \geqslant 0.8$.

In (7) the $P(\ell\,|\mathrm{QEL})$ and $P(\ell\,|\mathrm{BG})$ are the probabilities for signal and background events to have the values of the variables $\ell = (P_\perp^{\mathrm{mis}}, \theta_h, \alpha)$. We have found that the DIS and RES probability functions are very similar; therefore we build the likelihood function taking only resonance events for the denominator of (7).

---

[6]We also undertook an attempt to identify positively charged particles using the TRD information. A special algorithm [81, 82] can be potentially used for discrimination between two particle-ID hypotheses (p/π in our case). However, a low momentum ($\sim 0.9\,\mathrm{GeV}$) of the particle and a rather large emission angle ($\gtrsim 45°$) result in that either the particle does not reach the TRD or the number of residual TRD hits is not large enough for the identification. Therefore, the TRD algorithm could be applied only to a limited fraction of events ($\sim 6\%$) and cannot play any significant role in our analysis.

Table 4 Number of data N_{data} and renormalized MC N_{mc} events in ν_μ and $\bar{\nu}_\mu$ QEL samples; expected selection efficiency, purity and background contaminations (BG) for different stages of the analysis. Number of MC events N_{mc} were normalized to the N_{data} after the selection. Expected numbers of MC events were recalculated for the earlier stages of the analysis on the basis of this number

|	QEL eff. (%)	QEL purity (%)	RES BG (%)	DIS BG (%)	oth. BG (%)	N_{data}	N_{mc}
ν_μ 1-track before θ_h cut	23.7	29.0	18.3	52.3	0.4	16508	16633.7
ν_μ 1-track after θ_h cut	21.3	41.7	23.2	34.5	0.6	10358	10358.0
ν_μ 2-track after quality cuts	21.2	9.4	9.3	77.9	3.4	41768	44937.2
ν_μ 2-track after θ_h cut	18.4	36.2	18.0	45.6	0.2	10144	10355.6
ν_μ 2-track after $P_\perp^{mis}$ cut	18.2	40.8	18.8	40.1	0.3	9084	9082.8
ν_μ 2-track after α cut	17.6	47.2	17.3	35.2	0.3	7575	7609.0
ν_μ 2-track after $\mathcal{L}$ cut	13.3	73.9	10.2	15.8	<0.1	3663	3663.0
$\bar{\nu}_\mu$ 1-track before θ_h cut	81.8	29.8	22.8	45.8	1.6	3585	3555.8
$\bar{\nu}_\mu$ 1-track after θ_h cut	64.4	36.6	28.5	33.6	1.3	2237	2237.0
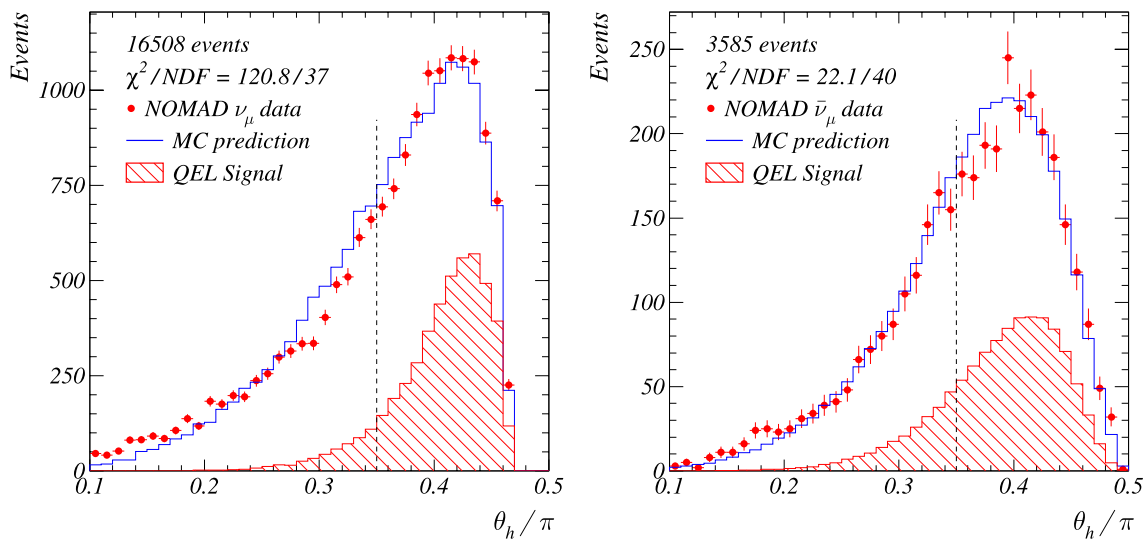
Fig. 11 The θ_h distributions for single track ν_μ (*left*) and $\bar{\nu}_\mu$ (*right*) samples: comparison of MC distributions (histograms) with the real data (points with error bars)

The comparison of $P_\perp^{mis}$, α, θ_h and $\mathcal{L}$ distributions in the data with the mixture of simulated QEL, RES and DIS events weighted by their flux-averaged cross sections is displayed in Fig. 10. The good agreement observed between MC predictions and experimental data confirms a reasonable understanding of the background contaminations and reconstruction efficiency in our analysis. For example, after the likelihood cut, the respective contributions of QEL, RES, DIS and COH given by the cross sections and the efficiencies computed with the help of the MC for each process separately are as specified on the corresponding $\mathcal{L} > 0$ line in Table 4. With the reduction factors for the $\mathcal{L} > 0$ cut as given by the MC in the various channels, and normalizing the total MC to the data at this last stage, we find a total of 7609 events before the cut, distrib-

uted as shown by the figures on the corresponding line. The excess of 34 MC events relative to the data, which are necessarily mostly background, can be taken as evidence that there is less than 1% excess background in the MC after the pre-cuts. Since the total MC background is of the order of 4000 events, the number found is well under the expected statistical fluctuations. Therefore, there is no evidence of a statistically significant discrepancy.

In the case of 1-track events, our abilities to suppress background contamination are limited since all kinematic variables are expressed in terms of the muon momentum p_μ and emission angle θ_μ with the help of the conservation laws for QEL events. Therefore, the proton reconstructed emission angle, (6), can be con-
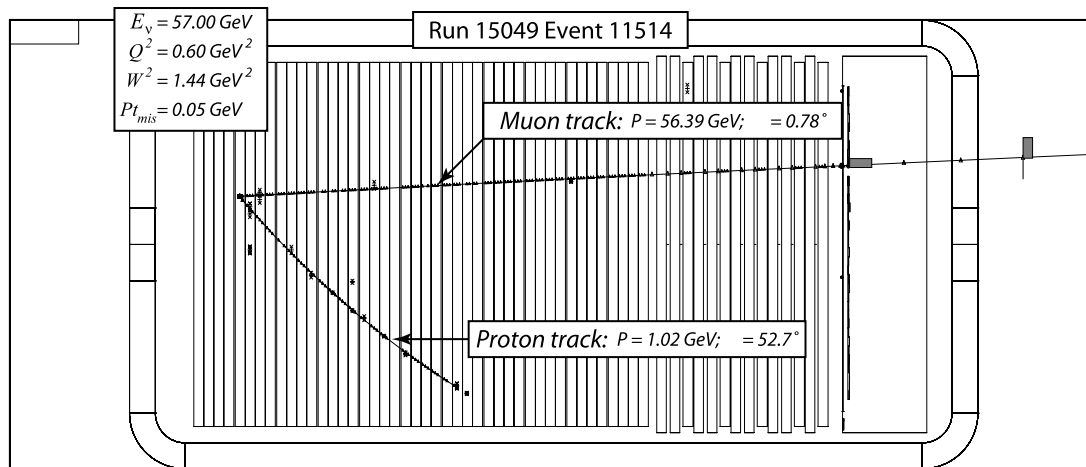
Fig. 12 A typical example of data event (run 15049 event 11514) identified as $\nu_\mu n \to \mu^- p$ in this analysis. The long track is identified as a muon, the short track is assumed to be a proton

sidered as an analog of the likelihood function (see Fig. 11).

The explicit values for the kinematic selection criteria ($\mathcal{L} \geqslant 0$ for the 2-track sample and $0.35 \leqslant \theta_h/\pi \leqslant 0.5$ for the 1-track sample) were found from the optimization of the sensitivity $\mathrm{SG}/\sqrt{\mathrm{SG} + \mathrm{BG}}$, where SG and BG are the expected numbers of signal and background events in the identified QEL sample.

5.2 $\bar{\nu}_\mu p \to \mu^+ n$ selection

The investigation of the antineutrino sample is a much simpler task since these events are mostly ($\sim$96% of cases) reconstructed as 1-track events (we have no hits from outgoing neutrons in the drift chambers). Therefore, we require identification of the positively charged muon and follow the procedure for the 1-track sample discussed above. The only difference is the absence of contamination from the inverse muon decay events, so we do not need to apply the quality cut on the transverse muon momentum.

In Table 4 we summarize the information about the selection of samples with $\nu_\mu n \to \mu^- p$ and $\bar{\nu}_\mu p \to \mu^+ n$ candidates in the data. The last two columns of this table allow us to make checks of compatibility between the levels of background in the data and in our simulations in a manner similar to what is explained above for the two track sample.

An example of the 2-track event from real data identified as $\nu_\mu n \to \mu^- p$ is displayed in Fig. 12.

6 The QEL cross section and axial mass measurements

In this section we describe our analysis procedure. The QEL cross section measurement using normalization either to the total (DIS) ν_μ ($\bar{\nu}_\mu$) CC cross section or to the inverse muon decay (IMD), $\nu_\mu e^- \to \mu^- \nu_e$, events is first presented in Sect. 6.1. Afterwards, we describe the procedure used to extract the value of the axial mass M_A from the fit of the Q^2 distribution. This is the subject of Sect. 6.2.

6.1 The QEL cross-section measurement

Since there was no precise knowledge of the integrated neutrino flux in the NOMAD experiment, we use a different process with a better known cross section, recorded at the same time, for the normalization of the QEL cross section. A similar procedure was often applied in previous neutrino experiments, as for example, CERN BEBC [18]. Moreover, the use of another process recorded in the same experimental runs allows one to reduce significantly the systematic uncertainty related to the detector material composition. Nevertheless, this auxiliary process must meet two requirements: its cross section should be measured with rather high accuracy and the corresponding events can easily be extracted from the full data sample.

Let us divide the investigated interval of neutrino energy into several bins and enumerate them with index $i = 1..N_E$. Then, the number of identified QEL events in the ith bin with boundaries $[E_i, E_{i+1}]$ is

$$N_i^{\text{dat}} = N_i^{\text{bg}} + C \sum_{j=1}^{N_E} \varepsilon_{ij}^{\text{qel}} \Phi_j \langle \sigma_{\text{qel}} \rangle_j, \tag{8}$$

where

$$\Phi_i = \int_{E_i}^{E_{i+1}} \Phi(E)\,dE, \quad \sum_{i=1}^{N_E} \Phi_i = 1$$

and

$$\langle\sigma_{\text{qel}}\rangle_i = \frac{1}{\Phi_i}\int_{E_i}^{E_{i+1}}\sigma_{\text{qel}}(E)\Phi(E)\,dE.$$

The coefficient C accumulates the absolute neutrino flux and the number of target nucleons. The matrix element $\varepsilon_{ij}^{\text{qel}}$ is the probability that the reconstructed neutrino energy E_ν of a QEL event falls into the ith bin, while the simulated energy actually belongs to the jth bin.

The expected background contamination is

$$N_i^{\text{bg}} = C\bigl(\varepsilon_i^{\text{res}}\langle\sigma_{\text{res}}\rangle + \varepsilon_i^{\text{dis}}\langle\sigma_{\text{dis}}\rangle\bigr) \qquad (9)$$

where we use the definition of (4) for $\langle\sigma_{\text{bg}}\rangle$; $\varepsilon_i^{\text{bg}}$ denotes the renormalized energy distribution in BG events passing the QEL identification procedure:

$$\sum_{i=1}^{N_E}\varepsilon_i^{\text{bg}} = \varepsilon^{\text{bg}} = N_{\text{rec}}^{\text{bg}}/N_{\text{sim}}^{\text{bg}}. \qquad (10)$$

Here $N_{\text{sim}}^{\text{bg}}$ and $N_{\text{rec}}^{\text{bg}}$ are the number of MC events simulated and identified as QEL in the chosen detector FV.

Similar equations can be written for any other process recorded in the same detector FV. If we identify N_0 events of a process, whose flux-averaged cross section in an energy interval containing these events is σ_0, we can write

$$N_0 = C\,\Phi_0\sigma_0,$$

where Φ_0 is the relative part of the neutrino flux belonging to the same energy interval. (we assume that N_0 is background subtracted and efficiency corrected).

We can now get rid of C and write the final equation for $\langle\sigma_{\text{qel}}\rangle_i$:

$$\langle\sigma_{\text{qel}}\rangle_i = \frac{1}{\Phi_i}\sum_{j=1}^{N_E}(\varepsilon_{\text{qel}}^{-1})_{ij}$$
$$\times\left[N_j^{\text{dat}}\frac{\Phi_0\sigma_0}{N_0} - \varepsilon_j^{\text{res}}\langle\sigma_{\text{res}}\rangle - \varepsilon_j^{\text{dis}}\langle\sigma_{\text{dis}}\rangle\right]. \qquad (11)$$

Numerical values for $\langle\sigma_{\text{res}}\rangle$ and $\langle\sigma_{\text{dis}}\rangle$ are given in Table 3. The efficiencies $\varepsilon_{ij}^{\text{qel}}$, $\varepsilon_i^{\text{res}}$ and $\varepsilon_i^{\text{dis}}$ should be estimated with the help of the MC simulation for QEL, RES and DIS samples separately; the factor $\Phi_0\sigma_0/N_0$ comes from the auxiliary process used for normalization.

Let us note that the smearing of the reconstructed neutrino energy is taken into account in (11) by the inverse matrix of QEL efficiencies.

Equation (11) can also be applied to the entire energy interval. In this case, we can use the usual notations for efficiencies as in (10). From the measured $\langle\sigma_{\text{qel}}\rangle$ we calculate the axial mass M_A by using the Smith and Moniz formalism (see Fig. 4).

In the following subsections, we investigate the DIS and IMD processes which can both be used for the QEL cross-section normalization as just described.

Possible sources of systematic errors in our analysis procedure are discussed in Sect. 7.

6.1.1 Selection of DIS events

The phenomenology of neutrino DIS is well developed. Experimental data are in rather good agreement with theoretical predictions. The charged-current neutrino DIS is an inclusive process and for its selection from the data sample, the following criteria are enough.

– *Fiducial volume cut.* The primary vertex should be in the same FV as that defined for the QEL events, see (5).
– *Muon identification and topology cut.* At least two charged tracks should originate from the primary vertex; one of them should be identified as a muon (μ^- in the case of ν_μ CC and μ^+ for $\bar\nu_\mu$ CC).
– *Background suppression.* The third criterion is used to avoid contributions from the QEL and RES events. We have checked three different possibilities for it.

1. The total visible energy in the event should be $E_\nu \leqslant 300$ GeV and the reconstructed hadronic mass $W \geqslant 1.4$ GeV; in this case the computation of $\langle\sigma_{\text{dis}}\rangle$ has been done for GRV98-LO PDF model according to the prescriptions in [65].
2. We keep the requirement for the reconstructed hadronic mass ($W \geqslant 1.4$ GeV) but reduce the neutrino energy region to $40 \leqslant E_\nu \leqslant 200$ GeV; theoretical calculation of $\langle\sigma_{\text{dis}}\rangle$ is also done with the help of [65].
3. Using the same neutrino energy interval as in 2 ($40 \leqslant E_\nu \leqslant 200$ GeV), we remove the cut on the reconstructed hadronic mass W. In this case, we take the total CC neutrino–nucleon cross section to be[7]

$$\sigma_\nu^{\text{tot}}(E_\nu)/E_\nu = (0.677 \pm 0.014) \times 10^{-38}\ \text{cm}^2/\text{GeV},$$
$$\sigma_{\bar\nu}^{\text{tot}}(E_\nu)/E_\nu = (0.334 \pm 0.008) \times 10^{-38}\ \text{cm}^2/\text{GeV}$$

(PDG average [49]). The calculated $\langle\sigma_{\text{tot}}\rangle$ should be corrected due to the fact that NOMAD target is slightly non-isoscalar (0.984 for ν_μ and 1.014 for $\bar\nu_\mu$).

The numerical results of the DIS events selection can be found in Table 5. For the QEL cross-section normalization we use results obtained with the last method (PDG based). Other two methods are also used in the analysis to control and minimize the overall systematic error on the final results. Thus, the final normalization is performed to the total

---

[7]The CHORUS measurement for the CH_2 target [83] is consistent with this value.

Table 5 Selection of the DIS events in ν_μ and $\bar{\nu}_\mu$ CC samples. Total efficiency (in %), expected purity of selected events (in %), theoretical prediction for $\langle\sigma_{\text{dis}}\rangle$, observed N_{dat} and corrected N_0 number of events in experimental data are given for each variant of DIS selection described above

Variant of DIS selection	ν_μ sample			$\bar{\nu}_\mu$ sample		
	1	2	3	1	2	3
Efficiency	82.95	86.84	88.52	75.46	81.40	83.20
Purity	97.10	98.62	99.62	71.48	72.57	73.95
N_{dat}, events	676702.0	267517.0	276018.0	17744.0	7996.0	8500.0
N_0, events	792162.0	303790.7	310617.3	16807.1	7128.6	7553.4
Relative flux Φ_0	1	0.144	0.144	1	0.106	0.106
$\langle\sigma_0\rangle$, 10^{-38} cm^2	16.643	44.876	46.069	4.876	20.124	21.999
C^{-1}, 10^{-43} cm^2	2.101	2.127	2.136	29.012	29.924	30.872

ν_μ ($\bar{\nu}_\mu$) CC cross section. We also checked that this normalization is consistent with two previous calculations based on approach from [65] within 1.6% (5.9%) for ν_μ ($\bar{\nu}_\mu$) CC sample.

6.1.2 Selection of inverse muon decay events

Inverse muon decay $\nu_\mu e^- \to \mu^- \nu_e$ is a purely leptonic process, which is well known both on theoretical and experimental grounds. Its cross section in the Born approximation is

$$\sigma_{\text{imd}}(E_\nu) = \sigma_{\text{as}} E_\nu \left(1 - \frac{m_\mu^2}{2m_e E_\nu}\right)^2. \tag{12}$$

The numerical value of the constant σ_{as} calculated in the framework of the Standard Model was found to be in good agreement with experimental measurements [84]:

$$\sigma_{\text{as}} = \frac{2m_e G_F^2}{\pi} = 1.723 \times 10^{-41} \text{ cm}^2 \text{ GeV}^{-1}. \tag{13}$$

The number of IMD events N_0 is proportional to its flux-averaged cross section from (4):

$$\langle\sigma_{\text{imd}}\rangle = 1.017 \times 10^{-40} \text{ cm}^2 \tag{14}$$

and expected to be at least 650 times smaller than the number of DIS events.

To select the IMD events we require:

– the primary vertex should be in the same fiducial volume as that used for identified QEL events, see (5);
– there is only one negatively charged track originating from the primary vertex; it should be identified as a muon;
• there are no veto chamber hits in the vicinity of the intersection point of the extrapolated muon track and the first drift chamber (quality cut, the same as for 1-track events from the QEL sample);
• the muon energy is above the threshold:

$$E_\mu \geqslant \frac{m_\mu^2 + m_e^2}{2m_e} = 10.93 \text{ GeV}; \tag{15}$$

– the transverse momentum $p_\perp$ of the muon produced in IMD event is very limited by kinematics: $p_\perp^2 \leqslant 2m_e E_\mu$.

In this sample the contamination from the reaction $\bar{\nu}_e e \to \mu^- \bar{\nu}_\mu$ is estimated to be at the level of $\sim 10^{-3}$, e.g. well below 1 event, since the ratio of the fluxes $\bar{\nu}_e/\nu_\mu$ is 0.0027 [30] while the ratio of the cross sections is $\sigma(\bar{\nu}_e e \to \mu^- \bar{\nu}_\mu)/\sigma(\nu_\mu e \to \mu^- \nu_e) \approx 1/3$.

We determine the number of signal events N_{imd} from the fit of the $p_\perp^2$ distribution to experimental data with the function $F(p_\perp^2)$:

$$F(p_\perp^2) = N_{\text{imd}} F_{\text{imd}}(p_\perp^2) + [N_{\text{dat}} - N_{\text{imd}}] F_{\text{bg}}(p_\perp^2), \tag{16}$$

where F_{imd} and F_{bg} are the normalized MC expectations for signal and background $p_\perp^2$ distributions; N_{dat} denotes the number of events in real data which passed all selection criteria.

The QEL events are now playing the role of the most important background for the IMD selection. However, the contaminations from the RES and DIS events cannot be neglected since they distort the shape of the $p_\perp^2$ distribution. As usual, the relative contribution of each process to the expected background is proportional to the corresponding efficiency and flux-averaged cross section (see Table 3).

The expression (16) contains only one free parameter N_{imd}, which is the number of observed IMD events. Finally, for $p_\perp^2 < 0.03$ (GeV/c)^2 interval we find $N_{\text{imd}} = 436.0 \pm 28.5$ with the quality of the fit $\chi^2/NDF = 0.89$ (see Fig. 13). Taking into account that the selection efficiency for the IMD events is 87.8% we report the total number of IMD events N_0, which can be used for the QEL normalization:

$$N_0 = 496.6 \pm 32.5. \tag{17}$$

The relative error for σ_0/N_0 in the IMD case is about 7% (due to the small statistics of the IMD sample). Nevertheless the normalization factor itself, $C^{-1} = 2.048 \times 10^{-43}$ cm^2, is in agreement (within ~ 4%) with the evaluation based on the DIS sample (see Table 5).

The use of the IMD process for the normalization is an interesting independent cross-check of the absence of problems in our procedure. In particular, it allows us to verify
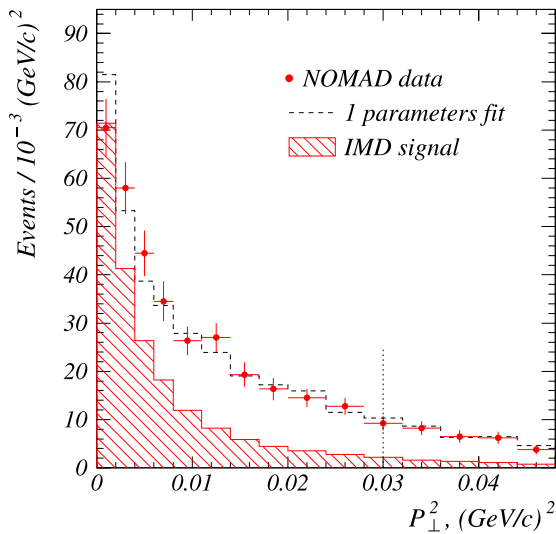
Fig. 13 Inverse Muon Decay: NOMAD experimental data, the $p_\perp^2$ distribution. Please note that the bins are of unequal widths: Bins 1 to 4, 5 to 8 and 9 to last are respectively 0.001, 0.0015 and 0.002 $(GeV/c)^2$ wide. Also note that the data above 0.03 were not used in the fit

that there are no effects arising from possible trigger inefficiencies in the selection of neutrino events consisting of a single muon going through the trigger planes.

6.2 Axial mass measurement from the Q^2 distribution

To extract the axial mass from the Q^2 distribution the experimental data are fitted to the theoretical predictions using a standard χ^2 method. We bin the events in two variables Q^2 and E_ν (in the case of a single E_ν interval our procedure can be considered as the usual 1-dimensional fit).[8]

Let us enumerate bins with index $i = 1..N_B$; bin $i = N_B + 1$ contains events which fall outside of the investigated (E_ν, Q^2) region. It is convenient to define boundaries in such a way that each bin with $i = 1..N_B$ contains approximately the same number of experimental events passing all identification criteria.

A minimization functional is:

$$\chi^2(M_A) = \sum_{i=1}^{N_B} \frac{[N_i^{\text{dat}} - N_i^{\text{th}}(M_A)]^2}{N_i^{\text{th}}(M_A)}, \qquad (18)$$

where N_i^{dat} is the number of events in the ith bin of the experimental distribution, while N_i^{th} is a superposition of the normalized MC background N_i^{bg} and the expected QEL sig-

nal:

$$N_i^{\text{th}}(M_A) = N_i^{\text{bg}} + C \sum_{j=1}^{N_B+1} \varepsilon_{ij}^{\text{qel}} \Phi_j \langle \tilde{\sigma}_{\text{qel}} \rangle_j. \qquad (19)$$

This equation is similar to (8), N_i^{bg} being defined in the same way as in (9); $\varepsilon_{ij}^{\text{qel}}$ is the probability that a QEL event simulated in the jth bin is reconstructed in the ith bin. The QEL scattering dynamics is described by the following term:

$$\langle \tilde{\sigma}_{\text{qel}} \rangle_i = \frac{1}{\Phi_i} \int_{\Omega_i} \frac{d\sigma}{dQ^2}(E, Q^2, M_A) \Phi(E) \, dE \, dQ^2, \qquad (20)$$

$$\Phi_i \langle \tilde{\sigma}_{\text{qel}} \rangle_i |_{i=N_B+1} = \langle \sigma_{\text{qel}} \rangle - \sum_{j=1}^{N_B} \Phi_j \langle \tilde{\sigma}_{\text{qel}} \rangle_j. \qquad (21)$$

Here Ω_i denotes the (E_ν, Q^2) interval, which corresponds to the ith bin; $d\sigma/dQ^2$ is the differential QEL cross section on bound target nucleon (see formulae in [32]).

The coefficient C can be defined in either of two ways:

1. the N_i^{th} distribution is normalized to the total number of events in the experimental data:

$$\sum_{i=1}^{N_B} N_i^{\text{th}} = \sum_{i=1}^{N_B} N_i^{\text{dat}}. \qquad (22)$$

In this case, the proposed method should be sensitive only to the shape of the distribution but not to the absolute number of identified events (contrary to the M_A measurement from the total QEL cross section).

2. C is defined in the same way as for the total QEL cross-section measurement, i.e. we use another process (DIS) for normalization:

$$C = \frac{N_0}{\Phi_0 \sigma_0}. \qquad (23)$$

If we sum over the Q^2 variable for the investigated (E_ν, Q^2) interval, finding the M_A parameter from (18) becomes nothing else than the numerical resolution of (8). Therefore, this variant of the fit can be considered as a simultaneous fit of the total and differential cross sections; henceforth, we shall refer to it as $\sigma \otimes d\sigma/dQ^2$ fit.

Figure 14 presents a comparison of the reconstructed Q^2 distribution with our MC prediction. The expected background contamination is also shown.

We can now apply the proposed methods to experimental data and measure the QEL cross section and axial mass M_A. The numerical results are reported in Sect. 8, while the discussion of the corresponding uncertainties is presented in the next section.

---

[8]In practice it is convenient to use dimensionless variables (a, b) instead of (E_ν, Q^2). Then, $E_\nu = E_\nu^{\text{min}} + a(E_\nu^{\text{max}} - E_\nu^{\text{min}})$ and $Q^2 = Q_{\text{min}}^2(E_\nu) + b[Q_{\text{max}}^2(E_\nu) - Q_{\text{min}}^2(E_\nu)]$. So, $a, b \in [0, 1]$.

7 Systematic uncertainties

We have studied several sources of systematic uncertainties, which are important for the measurement of the total QEL cross section and axial mass parameter. They are listed below.

1. Identification of QEL events; we vary the selection criteria within reasonable limits ($\mathcal{L} > 0 \pm 0.4$ for 2-track sample and $\theta_h/\pi > 0.35 \pm 0.03$ for 1-track sample).

   The final result is found to be practically insensitive to the exact positions of the muon azimuth φ_μ cut and additional requirements for the $P_\perp^{\mathrm{mis}}$, α and θ_h variables: e.g. in the ν_μ analysis a more strict cut $0.1\pi < \varphi_\mu < 0.9\pi$ leads to 0.8% variation in the measured cross sec-
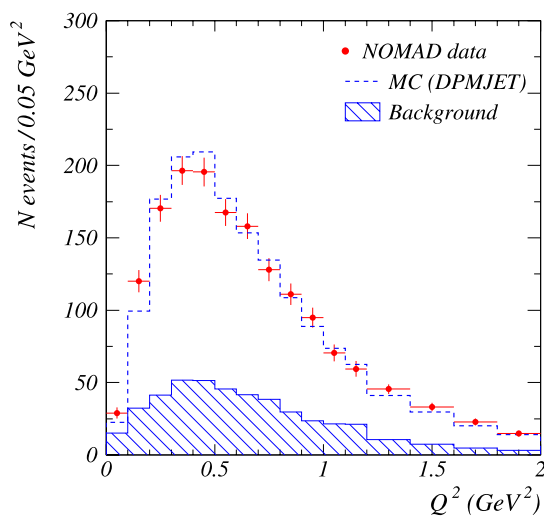
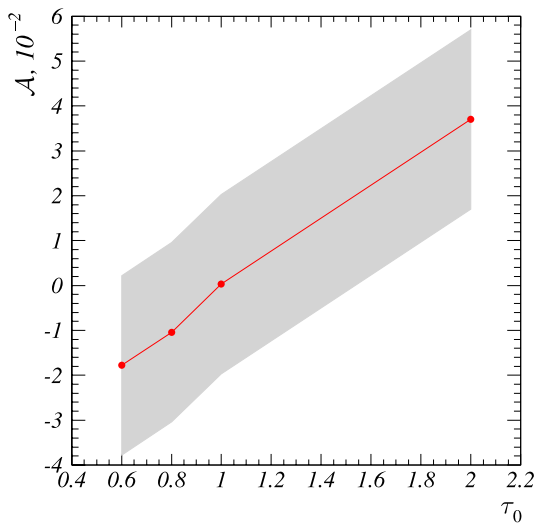**Fig. 14** The Q^2 distributions in identified QEL events

tion while a change in the pre-cuts to $P_\perp^{\mathrm{mis}} < 0.9$ GeV, $\alpha/\pi > 0.75$ and $0.18\pi < \theta_h$ leads to an uncertainty of 0.4%.

2. Uncertainty in the total (mainly DIS) charged-current muon neutrino cross section, which enters both in the normalization factor σ_0/N_0 and in the subtraction of the corresponding DIS background (the experimental error on $\langle\sigma_{\mathrm{dis}}\rangle$ is 2.1% for ν_μ CC and 2.4% for $\bar{\nu}_\mu$ CC).
3. Uncertainty in the RES cross section, which determines the contamination admixture of the single resonant pion events in the identified QEL sample (we assume 10% error on $\langle\sigma_{\mathrm{res}}\rangle$ both for neutrino and antineutrino cases, see e.g. [56]).
4. FSI interactions (we vary τ_0 and α_{mod}^F DPMJET parameters for fixed $M_A^{\mathrm{mc}} = 1.03$ GeV).
5. Uncertainty in the neutrino flux shape (the relative errors for each E_ν bin were taken from [30]).
6. Uncertainty, concerning to the axial mass value M_A^{mc}, used for MC production.
7. Neutral current admixture (we assume 5% error for the corresponding cross section, which can be found in Table 3).
8. Charge misidentification of the primary lepton (reconstructed ν_μ CC event is classified as $\bar{\nu}_\mu$ CC and vice versa).
9. Contamination from coherent pion production (see Sect. 4.4).

In Table 6 we present our numerical estimations for systematic uncertainties (in the case of ν_μ scattering, systematic errors were calculated for the mixture of 1-track and 2-track subsamples). One can see that the most important contributions come from the QEL identification procedure and from

Table 6 The relative systematic uncertainties (in %) of the QEL cross section $\langle\sigma_{\mathrm{qel}}\rangle$ and axial mass M_A, measured in $\nu_\mu n \to \mu^- p$ and $\bar{\nu}_\mu p \to \mu^+ n$ reactions

Source	$\langle\sigma_{\mathrm{qel}}\rangle_{\nu_\mu}$	M_A from $\langle\sigma_{\mathrm{qel}}\rangle_{\nu_\mu}$	M_A from $d\sigma_\nu/dQ^2$	$\langle\sigma_{\mathrm{qel}}\rangle_{\bar{\nu}_\mu}$	M_A from $\langle\sigma_{\mathrm{qel}}\rangle_{\bar{\nu}_\mu}$
1 QEL identification procedure:					
likelihood or θ_h cut	3.5	3.2	2.4	4.3	4.2
φ_μ cut	0.8	0.7	0.3	–	–
$P_\perp^{mis}$, α and θ_h precuts	0.4	0.4	0.4	–	–
2 $\delta(\langle\sigma_{dis}\rangle)$, $\delta(\sigma_0)$	2.9	2.6	0.2	4.2	4.2
3 $\delta(\langle\sigma_{res}\rangle)$	4.0	3.6	0.6	7.6	7.4
4 Nuclear reinteractions	1.8	1.6	6.5	–	–
5 Shape of neutrino spectrum ($\delta(\Phi)$)	1.6	1.5	0.1	5.9	5.6
6 $\delta(M_A^{mc})$	1.0	0.9	0.9	1.4	1.4
7 NC contribution	<0.1	<0.1	–	1.1	1.1
8 Muon misidentification	<0.1	<0.1	–	1.0	1.0
9 Coherent pion production	<0.1	<0.1	<0.1	1.1	1.1
Total	6.7	6.0	7.0	11.6	11.1

Fig. 15 The asymmetry $\mathcal{A}$ as a function of the formation time parameter τ_0

the uncertainty on the non-QEL processes contribution to the selected sample of signal events.

The nuclear reinteractions (FSI effect) significantly affect the neutrino sample only (see Table 9), while in the antineutrino case the influence of the nuclear reinteractions is expected to be negligible.

In the case of $\bar{\nu}_\mu$ QEL scattering one measures only the μ^+ in the final state, while the outgoing neutron is not seen. This event topology can be changed only in the case of charged particle production through the intra-nuclear cascade. The fraction of those events is very small according to our MC estimations.

For ν_μ scattering, the cross sections can be calculated separately for both the 1-track and 2-track subsamples of identified QEL events or for their mixture. We can then compare the results and choose whichever one has the minimal total error. In our case it was obtained for the combined 1-track and 2-track sample, which was found to be almost insensitive to the variation of DPMJET parameters (see Sect. 8 for explanations).

In order to estimate the error due to the FSI modeling we consider the following asymmetry ratio:

$$\mathcal{A} = \frac{\sigma_1 - \sigma_2}{2(\sigma_1 + \sigma_2)}, \tag{24}$$

where σ_1 and σ_2 denotes to the ν_μ QEL cross sections calculated from the 1-track and 2-track subsamples respectively. The systematic errors in the measured σ_1 and σ_2 cross sections (here we take into account all possible sources of uncertainties, listed above, except FSI effects) provide an uncertainty in $\mathcal{A}$ which is found to be equal $\sim$0.02. The dependence of the asymmetry ratio $\mathcal{A}$ on the τ_0 parameter is shown in Fig. 15. One can conclude that allowed bounds

for the formation time parameter are $\tau_0 = 1.0 \pm 0.5$. It was also found that the final results are not very sensitive to modifications of the second parameter of the DPMJET package—α_{mod}^F. Using the default values $M_A^{\mathrm{mc}} = 1.03$ GeV, $\alpha_{\mathrm{mod}}^F = 0.6$ and varying τ_0 within the interval [0.5, 1.5] one can obtain the systematic uncertainty for the measured QEL neutrino cross section and axial mass value due to the modeling of FSI effects.

The uncertainty on the shape of the (anti)neutrino spectrum is important for the measurement of σ_{qel} as a function of neutrino energy E_ν. But it does not affect both the flux-averaged cross section $\langle \sigma_{\mathrm{qel}} \rangle$ and the M_A extraction from the Q^2 distribution.

The uncertainty due to the primary lepton misidentification and neutral currents comes into play through the subtraction of the corresponding background from the selected DIS sample, that is, from the normalization factor. The admixture of those events into the identified QEL events is negligible.

8 Results

8.1 $\nu_\mu n \to \mu^- p$ sample

The results of our analysis for the ν_μ sample are summarized in Table 9. We measure the flux-averaged QEL cross section in the neutrino energy interval 3–100 GeV (see (11)) for the 1-track and 2-track samples as well as for their mixture (which is called *Combined* in Table 9). For each $\langle \sigma_{\mathrm{qel}} \rangle$ we calculate the corresponding axial mass value, M_A. Results on M_A extraction both from the standard Q^2 fit and from the combined $\sigma \otimes d\sigma/dQ^2$ fit are also given. These measurements are repeated for several QEL MC with different values of input parameters (the axial mass M_A was varied between 0.83 and 1.23 GeV in steps of 0.1 GeV; the formation time τ_0 was allowed to take a value of 0.6, 1.0 and 2.0; the correction factor α_{mod}^F was varied within the interval [0.54, 0.69]). On top of this the NUANCE QEL MC with its own treatment of FSI effects is used for cross-checks.

We then observe that M_A recalculated from the measured $\langle \sigma_{\mathrm{qel}} \rangle$ depends on τ_0 if one refers to the 1-track or the 2-track samples. Specifically, the measured M_A value increases with increasing τ_0 when extracted from the 1-track sample while it decreases when extracted from the 2-track sample. This can be understood if we take into account the fact that the τ_0 parameter controls the probability for an outgoing nucleon to be involved in an intranuclear cascade. Increasing τ_0 then increases the fraction of QEL events with reconstructed proton and thus populates the 2-track sample to the detriment of the 1-track sample. This is the reason for the systematic overestimation of M_A extracted from the 1-track sample alone and its underestimation when extracted from the

Fig. 16 Comparison of our $\langle \sigma_{qel} \rangle_{\nu_\mu}$ measurements as a function of the neutrino energy in the 1-track and 2-track subsamples (for the best parameter $\tau_0 = 1.0$) with the final $\langle \sigma_{qel} \rangle_{\nu_\mu}$ values measured using the full event sample; see Table 7. An artificial shift is applied for the neutrino energy to make the overlapping points visible
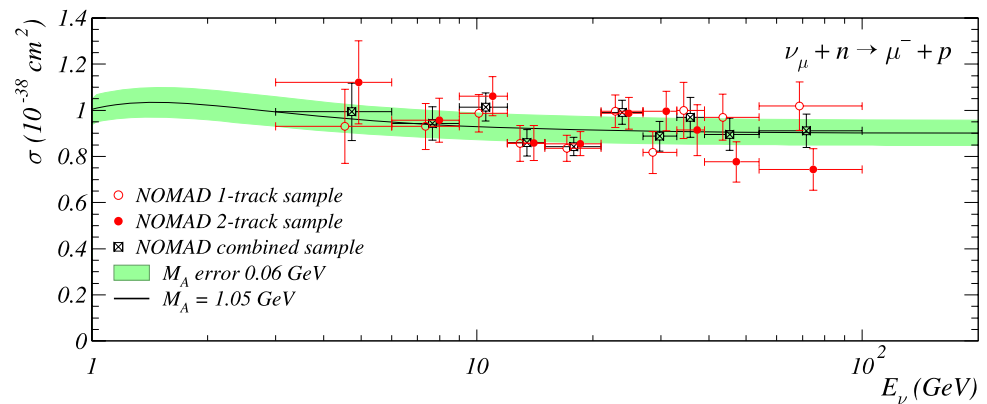
2-track sample alone. However the value of M_A extracted from the combination of the 1-track and 2-track samples is almost insensitive to variations of the τ_0 parameter.

We also find that using the QEL Monte Carlo with $\tau_0 = 1$ and $\alpha^F_{mod} = 0.6$ provides the most accurate prediction for the ratio between the 1-track and 2-track samples (and hence the most adequate description of the FSI): in this case the flux-averaged QEL cross section stays approximately the same whether measured from the 1-track sample or from the 2-track sample (see Table 9). This allows us to exclude the MC sets with $\tau_0 = 0.6$ and 2.0 from further considerations.

Figure 16 shows a comparison of our $\langle \sigma_{qel} \rangle_{\nu_\mu}$ measurements as a function of the neutrino energy in the 1-track and 2-track subsamples (for the best parameter $\tau_0 = 1.0$) with the final $\langle \sigma_{qel} \rangle_{\nu_\mu}$ values measured using the full event sample.

Similarly we have observed that when using the full sample (1-track and 2-track) the measured M_A is not very sensitive to modifications of the α^F_{mod} parameter. And using the NUANCE simulation code as a cross check gives a very consistent picture: the M_A value extracted from the 1-track sample is also different from the one extracted from the 2-track sample, while the value obtained with the combined sample nicely agrees with our measurement with the best FSI parameters. Thus, our results for the neutrino case are

$$\langle \sigma_{qel} \rangle_{\nu_\mu} = \left(0.92 \pm 0.02(\text{stat}) \pm 0.06(\text{syst})\right) \times 10^{-38} \text{ cm}^2,$$

$$M_A = 1.05 \pm 0.02(\text{stat}) \pm 0.06(\text{syst}) \text{ GeV}.$$

$$(25)$$

This result (25) is indeed in agreement with both the standard fit of the Q^2 distribution:

$$M_A = 1.07 \pm 0.06(\text{stat}) \pm 0.07(\text{syst}) \text{ GeV} \qquad (26)$$

and the fit of the combined $\sigma \otimes d\sigma/dQ^2$ distribution of the NOMAD data:

$$M_A = 1.06 \pm 0.02(\text{stat}) \pm 0.06(\text{syst}) \text{ GeV} \qquad (27)$$

(see Table 9, these results are obtained with a QEL MC using $M_A = 1.03$ GeV).

We use the 2-track sample only to extract M_A from the fit of the Q^2 distribution since in this case the purity of QEL identification is rather high ($\sim 74\%$, see Table 4). The results depend on the input MC parameters (axial mass and formation time) but still are in nice agreement with the results of the extraction of M_A from the measured QEL cross section based also on a 2-track sample analysis. This can be considered as an additional confidence for our measurements using the full QEL sample.

The measured cross section of the $\nu_\mu n \to \mu^- p$ reaction as a function of the neutrino energy is presented in Table 7 and is shown in Figs. 17 and 18. These results are compared to the previous measurements performed with deuterium and heavy nuclei targets (see discussion in Sect. 2).

8.2 $\bar{\nu}_\mu p \to \mu^+ n$ sample

In the $\bar{\nu}_\mu$ case the event topology is just a single μ^+, thus the uncertainties in the treatment of FSI effect almost do not influence the event selection. Since our measurement of the cross section of the $\bar{\nu}_\mu p \to \mu^+ n$ reaction is based on a 1-track sample only, we do not show the dependence of the results on the variation of the τ_0 and α^F_{mod} parameters. Instead we display a dependence on the input M_A in Table 10. The results for the measured M_A are found to be quite stable. In Fig. 19 we show the measured $\bar{\nu}_\mu p \to \mu^+ n$ cross section as a function of the antineutrino energy superimposed with the theoretical curve drawn with $M_A = 1.06 \pm 0.14$ GeV and with nuclear effects according to the standard relativistic Fermi gas model. Table 8 summarizes our results for the $\bar{\nu}_\mu p \to \mu^+ n$ cross-section measurement in the different antineutrino energy intervals. The cross sections are measured on a carbon target and also recalculated for a free nucleon. The statistical and systematic errors are both provided. The observed number of events in the data, the predicted number of background events, the background subtracted and efficiency corrected number of events are also shown.

Table 7 Cross section of quasi-elastic neutrino scattering (in units of 10^{-38} cm^2, statistical and systematic errors). σ_{carbon} is measured for the NOMAD nuclear target and normalized per 1 neutron; $\sigma_{\text{Free}} = \sigma_{\text{Nucl}}/g$ is the cross section for the free target neutron (the factor g is calculated according to the Smith–Moniz model; see [32]). The number of

selected events in raw data N_{dat}, the estimated background contamination N_{bg} and the number of events N_{cor} corrected for background and efficiency are also reported. The difference in the total number of data events with respect to Table 4 (13683 versus 14021) is due to the additional cut on the neutrino energy $3 < E_\nu(\text{GeV}) < 100$

E_ν	$\langle E_\nu \rangle$	N_{dat}	N_{bg}	N_{cor}	$(\sigma \pm \delta\sigma_{\text{stat}} \pm \delta\sigma_{\text{syst}})_{\text{Nucl}}$	$(\sigma \pm \delta\sigma_{\text{stat}} \pm \delta\sigma_{\text{syst}})_{\text{Free}}$
3–6	4.7	396	211.6	660.6	0.994 0.125 0.078	1.057 0.133 0.083
6–9	7.7	1115	580.2	1663.4	0.942 0.072 0.078	1.001 0.077 0.083
9–12	10.5	1683	835.3	2591.1	1.014 0.061 0.075	1.077 0.065 0.080
12–15	13.5	1647	834.9	2310.7	0.859 0.057 0.070	0.913 0.060 0.075
15–21	17.8	2815	1451.6	3766.8	0.843 0.040 0.067	0.896 0.043 0.071
21–27	23.8	2040	956.2	3084.7	0.991 0.052 0.070	1.053 0.055 0.075
27–33	29.8	1279	610.5	1816.8	0.888 0.064 0.073	0.943 0.068 0.077
33–39	35.8	852	400.9	1246.2	0.970 0.086 0.078	1.030 0.091 0.083
39–54	45.3	1008	496.1	1397.8	0.896 0.070 0.074	0.951 0.074 0.078
54–100	71.7	848	416.9	1191.5	0.911 0.073 0.077	0.967 0.078 0.082
3–100	23.4	13683	6794.2	19718.2	0.919 0.017 0.060	0.976 0.018 0.063

**Table 8** The same as Table 7 but for the antineutrino

E_ν	$\langle E_\nu \rangle$	N_{dat}	N_{bg}	N_{cor}	$(\sigma \pm \delta\sigma_{\text{stat}} \pm \delta\sigma_{\text{syst}})_{\text{Nucl}}$	$(\sigma \pm \delta\sigma_{\text{stat}} \pm \delta\sigma_{\text{syst}})_{\text{Free}}$
3–6	4.5	291	176.4	181.9	0.585 0.097 0.079	0.639 0.106 0.086
6–9	7.4	292	182.6	159.5	0.710 0.125 0.093	0.767 0.135 0.100
9–15	11.8	464	286.2	254.1	0.851 0.114 0.096	0.913 0.122 0.103
15–24	19.0	425	274.0	210.8	0.822 0.125 0.095	0.878 0.134 0.102
24–42	31.5	411	252.5	223.0	1.009 0.141 0.098	1.075 0.150 0.104
42–100	60.1	288	181.9	145.9	0.993 0.173 0.099	1.056 0.184 0.105
3–100	19.7	2171	1353.6	1182.5	0.811 0.053 0.081	0.866 0.056 0.086
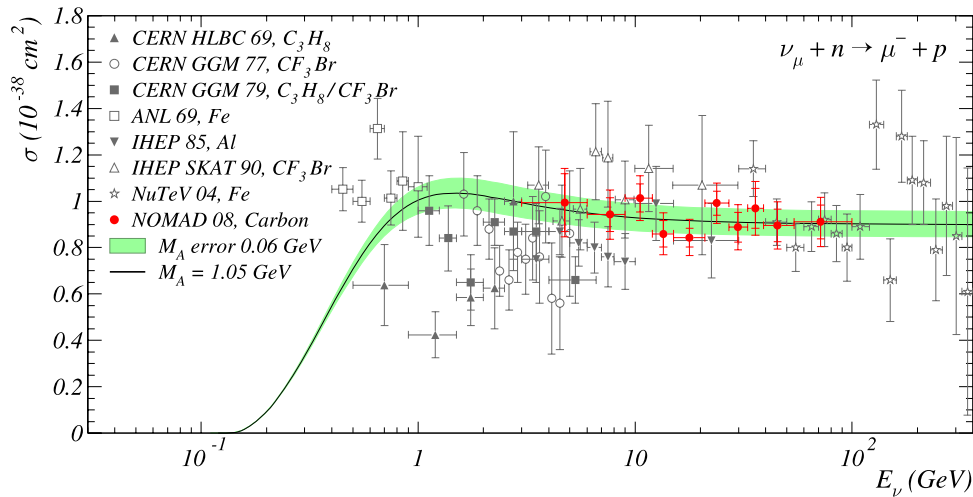
Fig. 17 Comparison of NOMAD $\langle \sigma_{\text{qel}} \rangle_{\nu_\mu}$ measurements with previous experimental data on ν_μ scattering off heavy nuclei (ANL 69 (Spark-chamber) [1], NuTeV 04 (FermiLab) [23], CERN HLBC 69 (CERN, Heavy Liquid Bubble Chamber) [14], CERN GGM 77 (CERN, Gargamelle BC) [15], CERN GGM 79 [17], IHEP 85 (IHEP, spark-chamber) [20], IHEP SCAT 90 (IHEP, BC) [22]). The *solid*

line corresponds to the calculations according to the relativistic Fermi gas model by Smith and Moniz [72] for carbon (with binding energy $E_b = 25.6$ MeV and Fermi momentum $P_F = 221$ MeV/c) using the M_A value obtained in the NOMAD experiment. The *error band* takes into account both statistical and systematic uncertainties of the present analysis
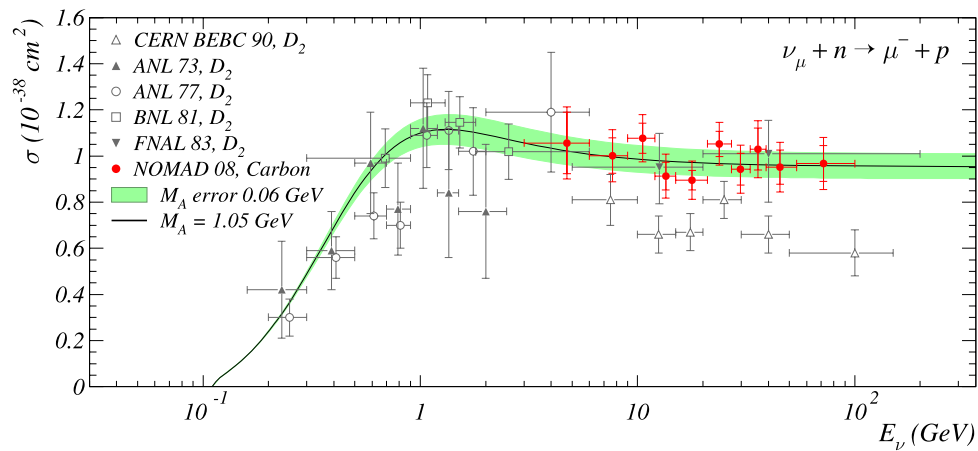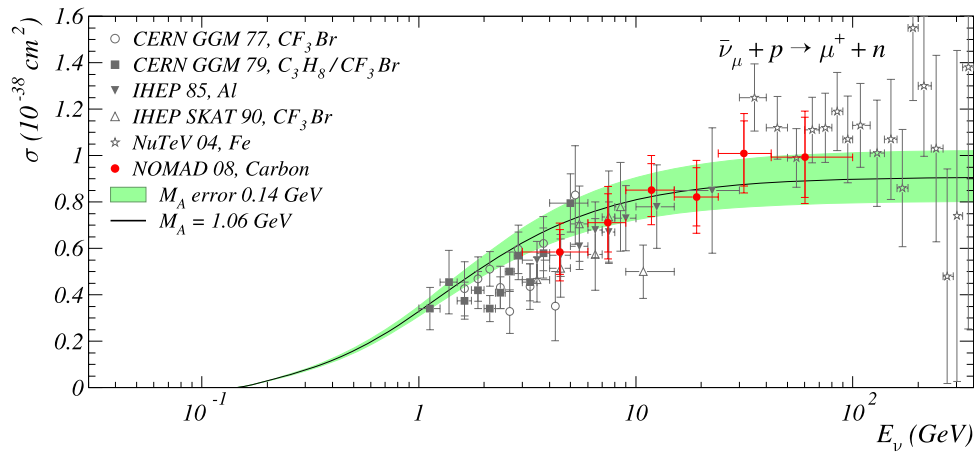
Fig. 18 Comparison of NOMAD $\langle\sigma_{\text{qel}}\rangle_{\nu_\mu}$ measurements with previous $\nu_\mu D$ experimental data (ANL 73 (Argonne 12-foot BC) [2], ANL 77 [3], BNL 81 (Brookhaven 7-foot BC) [6], FNAL 83 (FermiLab 15-foot BC) [9], BEBC 90 (CERN, Big European Bubble Chamber) [18]; corrections for nuclear effects have been made by the authors of the experiments). NOMAD measurements were divided by a factor $g = \sigma_{\text{Nucl}}/\sigma_{\text{Free}}$ which was calculated according to the Smith-Moniz model (see [32]). The *solid line* and *error band* corresponds to the M_A value obtained in the NOMAD experiment

Table 9 Parameters of the QEL MC simulation (axial mass M_A^{mc} and parameters of FSI modeling) are listed in the first three columns. The intermediate columns contain results of the QEL ν_μ cross-section measurement (in units of 10^{-38} cm^2, without errors) for the different topology of identified events (with or without reconstructed proton track). The axial mass value obtained from the fit of Q^2 distribution and $\sigma \otimes d\sigma/dQ^2$ fit ($Q_{\text{lim}}^2 = 0.2$–4 GeV^2) are given in the *last columns* of the table; only the statistical errors for the axial mass were shown. One can see that the final M_A measurement for the combined sample has a very weak dependence on the initial M_A^{mc} used in the simulation (e.g. variation of M_A^{mc} in a rather large interval from 0.83 to 1.23 leads to a variation of the measured M_A of about 0.03)

MC parameters			Single track		Two tracks		Combined		Fit of Q^2 distribution		Fit of $\sigma \otimes d\sigma/dQ^2$	
τ_0	α_{mod}^F	M_A^{mc}	σ_{qel}	M_A	σ_{qel}	M_A	σ_{qel}	M_A	$M_A \pm \delta M_A$	χ^2	$M_A \pm \delta M_A$	χ^2
0.60	0.60	0.83	0.863	0.990	1.014	1.148	0.915	1.047	1.113 0.057	19.4	1.105 0.018	19.3
1.00	0.60	0.83	0.885	1.015	0.956	1.090	0.912	1.043	1.095 0.057	11.6	1.058 0.018	11.9
2.00	0.60	0.83	0.918	1.050	0.851	0.977	0.892	1.021	0.960 0.093	17.4	0.965 0.018	17.4
0.60	0.60	0.93	0.882	1.011	1.015	1.148	0.928	1.061	1.135 0.056	10.0	1.119 0.018	10.0
1.00	0.60	0.93	0.893	1.023	0.942	1.074	0.911	1.043	1.075 0.060	13.5	1.065 0.018	13.5
2.00	0.60	0.93	0.931	1.063	0.844	0.968	0.896	1.026	1.009 0.069	12.2	0.971 0.018	12.4
0.60	0.60	1.03	0.910	1.041	0.977	1.110	0.935	1.067	1.016 0.051	25.8	1.094 0.017	27.1
1.00	0.60	1.03	0.919	1.051	0.918	1.050	0.919	1.051	1.073 0.059	18.7	1.059 0.018	18.7
2.00	0.60	1.03	0.950	1.083	0.819	0.939	0.896	1.026	0.993 0.079	18.4	0.968 0.018	18.4
0.60	0.60	1.13	0.946	1.079	0.979	1.113	0.959	1.092	1.031 0.077	24.9	1.109 0.017	26.4
0.80	0.60	1.13	0.948	1.081	0.926	1.058	0.940	1.073	1.092 0.056	13.8	1.079 0.018	13.8
1.00	0.60	1.13	0.962	1.096	0.904	1.035	0.940	1.072	1.100 0.062	19.4	1.060 0.018	19.6
2.00	0.60	1.13	0.995	1.129	0.789	0.904	0.906	1.037	0.999 0.080	18.0	0.956 0.018	18.2
0.60	0.60	1.23	0.994	1.127	0.925	1.058	0.967	1.100	1.039 0.053	20.7	1.088 0.018	21.2
0.80	0.60	1.23	0.996	1.129	0.904	1.035	0.959	1.092	1.013 0.039	21.1	1.066 0.017	21.7
1.00	0.60	1.23	1.000	1.134	0.879	1.008	0.951	1.085	0.970 0.087	20.1	1.051 0.017	21.3
2.00	0.60	1.23	1.038	1.171	0.777	0.889	0.921	1.053	0.996 0.079	20.9	0.964 0.018	16.3
0.80	0.54	1.03	0.921	1.053	0.963	1.097	0.937	1.070	1.113 0.054	20.9	1.079 0.018	21.1
0.80	0.57	1.03	0.921	1.052	0.950	1.083	0.932	1.064	1.072 0.062	15.5	1.067 0.018	15.5
0.80	0.60	1.03	0.920	1.051	0.959	1.092	0.935	1.067	1.090 0.064	12.7	1.089 0.018	12.7
0.80	0.63	1.03	0.912	1.044	0.953	1.087	0.928	1.060	1.082 0.062	15.8	1.084 0.018	15.7
0.80	0.66	1.03	0.905	1.035	0.933	1.066	0.916	1.047	0.989 0.091	19.9	1.067 0.017	20.9
0.80	0.69	1.03	0.904	1.035	0.940	1.072	0.918	1.049	0.937 0.113	15.7	1.070 0.017	18.0

Fig. 19 Comparison of NOMAD $\langle\sigma_{\mathrm{qel}}\rangle_{\bar{\nu}_\mu}$ measurements, Table 8, with previous experimental data on $\bar{\nu}_\mu$ scattering off heavy nuclei (CERN GGM 77 [15], CERN GGM 79 [16], IHEP 85 [20], IHEP SCAT 90 [22] and NuTeV 04 [23]). The *solid line* corresponds to the calculations according to the relativistic Fermi gas model by Smith and Moniz using the M_A value obtained in the NOMAD experiment. The *error band* takes into account both statistical and systematic uncertainties of the present analysis

Table 10 The results of QEL $\bar{\nu}_\mu$ cross-section measurement. The parameters of the DPMJET model are $\tau_0 = 1.0$, $\alpha_{\mathrm{mod}}^F = 0.6$

M_A^{mc}	σ_{qel}	M_A
0.83	0.794	1.042
0.93	0.799	1.048
1.03	0.811	1.063
1.13	0.834	1.094
1.23	0.861	1.127

Our final results for the antineutrino case are

$$\langle\sigma_{\mathrm{qel}}\rangle_{\bar{\nu}_\mu} = (0.81 \pm 0.05(\mathrm{stat}) \pm 0.09(\mathrm{syst})) \times 10^{-38} \ \mathrm{cm}^2,$$

$$M_A = 1.06 \pm 0.07(\mathrm{stat}) \pm 0.12(\mathrm{syst}) \ \mathrm{GeV}. \qquad (28)$$

9 Conclusions

The cross-section measurement of the $\nu_\mu n \to \mu^- p$ and $\bar{\nu}_\mu p \to \mu^+ n$ reactions on nuclear target was performed and reported in this article. The samples used in the analysis consist of 14,021 neutrino and 2,237 antineutrino events, which were identified as quasi-elastic neutrino scattering among the experimental data collected by the NOMAD Collaboration.

We have discussed in details the analysis procedure and the most significant sources of systematic error. Special attention was paid to the influence of the FSI effects on the measured physical quantities. The DPMJET code was used to simulate these FSI effects. We also proposed a method for tuning the intranuclear cascade parameters (mainly the formation time τ_0), which was then used to reduce the corresponding systematic uncertainty.

For the ν_μ case stable results have been obtained with the combined 1-track and 2-track samples since they are almost insensitive to the FSI effects.

The results for the flux-averaged QEL cross sections in the (anti)neutrino energy interval 3–100 GeV are

$$\langle\sigma_{\mathrm{qel}}\rangle_{\nu_\mu} = (0.92 \pm 0.02(\mathrm{stat}) \pm 0.06(\mathrm{syst})) \times 10^{-38} \ \mathrm{cm}^2$$

and

$$\langle\sigma_{\mathrm{qel}}\rangle_{\bar{\nu}_\mu} = (0.81 \pm 0.05(\mathrm{stat}) \pm 0.09(\mathrm{syst})) \times 10^{-38} \ \mathrm{cm}^2$$

for neutrino and antineutrino, respectively.

The axial mass M_A was calculated from the measured cross sections: we find $M_A = 1.05 \pm 0.06$ GeV from the ν_μ sample and $M_A = 1.06 \pm 0.14$ GeV from the $\bar{\nu}_\mu$ sample. The M_A parameter was also extracted from the fit of the Q^2 distribution in the high purity sample of ν_μ quasi-elastic 2-track events (with a reconstructed proton track). It was found to be consistent with the values calculated from the cross sections.

Our results are in agreement with the existing world average value [33, 36] and do not support the results found in recent measurements from the NuTeV [23], K2K [24, 25] and MiniBooNE [26] Collaborations, which reported somewhat larger values, however still compatible with our results within their large errors. A summary of existing experimental data on the axial mass measurements in neutrino and antineutrino experiments is shown in Fig. 20.

It should also be noted that the preliminary results reported earlier by the NOMAD Collaboration for the 2-track sample only [85, 86] suffered from a large systematic bias related to an improper treatment of the FSI effects in the simulation program. They should be now superseded by the new measurements reported here.
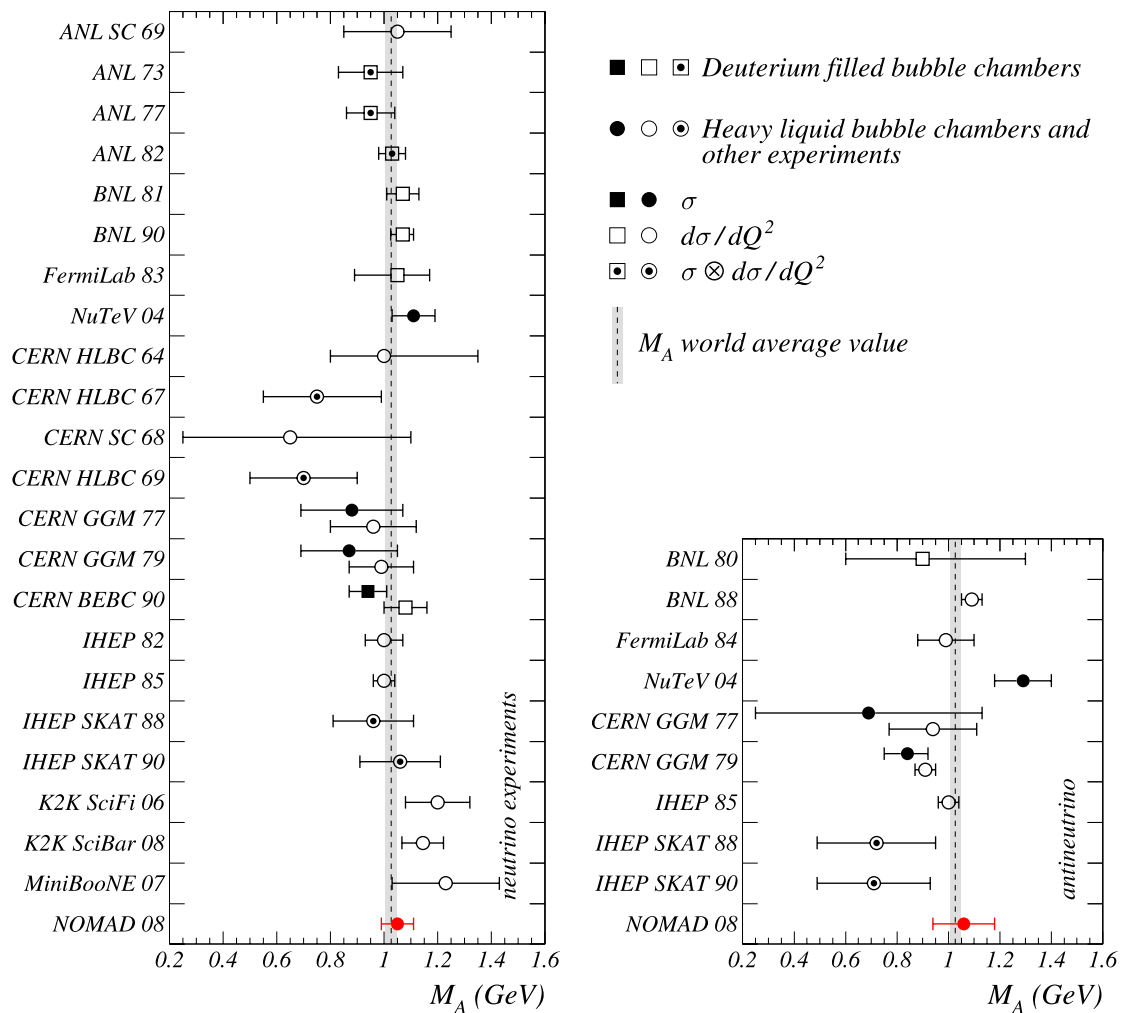
Fig. 20 A summary of existing experimental data: the axial mass M_A as measured in neutrino (*left*) and antineutrino (*right*) experiments. Points show results obtained both from deuterium filled BC (*squares*) and from heavy liquid BC and other experiments (*circles*). The *dashed line* corresponds to the so-called world average value $M_A = 1.026 \pm 0.021$ GeV (see the review in [33])

References

1. R.L. Kustom, D.E. Lundquist, T.B. Novey, A. Yokosawa, F. Chilton, Phys. Rev. Lett. **22**, 1014 (1969)
2. W.A. Mann et al., Phys. Rev. Lett. **31**, 844 (1973)
3. S.J. Barish et al., Phys. Rev. D **16**, 3103 (1977)
4. K.L. Miller et al., Phys. Rev. D **26**, 537 (1982)
5. G. Fanourakis et al., Phys. Rev. D **21**, 562 (1980)
6. N.J. Baker et al., Phys. Rev. D **23**, 2499 (1981)
7. L.A. Ahrens et al., Phys. Lett. B **202**, 284 (1988)
8. T. Kitagaki et al., Phys. Rev. D **42**, 1331 (1990)
9. T. Kitagaki et al., Phys. Rev. D **28**, 436 (1983)
10. A.E. Asratian et al., Phys. Lett. B **137**, 122 (1984)
11. M.M. Block et al., Phys. Lett. **12**, 281 (1964)
12. A. Orkin-Lecourtois et al., Nuovo Cimento A **50**, 927 (1967)
13. M. Holder et al., Nuovo Cimento A **57**, 338 (1968)
14. I. Budagov et al., Lett. Nuovo Cimento **2**, 689 (1969)

15. S. Bonetti et al., Nuovo Cimento A **38**, 260 (1977)
16. N. Armenise et al., Nucl. Phys. B **152**, 365 (1979)
17. M. Pohl et al., Lett. Nuovo Cimento **26**, 332 (1979)
18. D. Allasia et al., Nucl. Phys. B **343**, 285 (1990)
19. S.V. Belikov et al., Yad. Fiz. **35**, 59 (1982)
20. S.V. Belikov et al., Z. Phys. A **320**, 625 (1985)
21. H.J. Grabosch et al., Sov. J. Nucl. Phys. **47**, 1032 (1988)
22. J. Brunner et al., Z. Phys. C **45**, 551 (1990)
23. N. Suwonjandee, Ph.D. Thesis, University of Cincinnati (2004)
24. R. Gran et al., Phys. Rev. D **74**, 052002 (2006). arXiv:hep-ex/0603034 (K2K Collaboration)
25. C. Mariani, AIP Conf. Proc. **981**, 247 (2008) (K2K Collaboration)
26. A.A. Aguilar-Arevalo et al., Phys. Rev. Lett. **100**, 032301 (2008). arXiv:0706.0926 [hep-ex] (MiniBooNE Collaboration)
27. A.A. Aguilar-Arevalo et al., arXiv:hep-ex/0601022 (SciBooNE Collaboration) (2006)
28. D. Drakoulakos et al., arXiv:hep-ex/0405002 (Minerva Collaboration) (2004)
29. J. Altegoer et al., Nucl. Instrum. Meth. A **404**, 96 (1998) (NOMAD Collaboration)
30. P. Astier et al., Nucl. Instrum. Meth. A **515**, 800 (2003). arXiv:hep-ex/0306022 (NOMAD Collaboration)
31. V.V. Lyubushkin, Ph.D. Thesis, JINR, Dubna (2008)
32. K.S. Kuzmin, V.V. Lyubushkin, V.A. Naumov, Eur. Phys. J. C **54**, 517 (2008). arXiv:0712.4384 [hep-ph]
33. V. Bernard, L. Elouadrhiri, U.G. Meissner, J. Phys. G **28**, R1 (2002). arXiv:hep-ph/0107088
34. H. Budd, A. Bodek, J. Arrington, arXiv:hep-ex/0308005 (2003)
35. H. Budd, A. Bodek, J. Arrington, Nucl. Phys. Proc. Suppl. **139**, 90 (2005). arXiv:hep-ex/0410055
36. A. Bodek, S. Avvakumov, R. Bradford, H. Budd, Eur. Phys. J. C **53**, 349 (2008). arXiv:0708.1946 [hep-ex]
37. M. Anfreville et al., Nucl. Instrum. Meth. A **481**, 339 (2002). arXiv:hep-ex/0104012
38. G. Bassompierre et al., Nucl. Instrum. Meth. A **403**, 363 (1998)
39. G. Bassompierre et al., Nucl. Instrum. Meth. A **411**, 63 (1998)
40. J. Altegoer et al., Nucl. Instrum. Meth. A **428**, 299 (1999) (NOMAD Collaboration)
41. D. Autiero et al., Nucl. Instrum. Meth. A **373**, 358 (1996)
42. D. Autiero et al., Nucl. Instrum. Meth. A **411**, 285 (1998)
43. P. Astier et al., Nucl. Phys. B **611**, 3 (2001). arXiv:hep-ex/0106102 (NOMAD Collaboration)
44. P. Astier et al., Phys. Lett. B **570**, 19 (2003). arXiv:hep-ex/0306037 (NOMAD Collaboration)
45. C.H. Llewellyn Smith, Phys. Rep. **3**, 261 (1972)
46. M.F. Gari, W. Kruempelmann, Phys. Lett. B **274**, 159 (1992)
47. E.L. Lomon, Phys. Rev. C **66**, 045501 (2002). arXiv:nucl-th/0203081
48. E.L. Lomon, arXiv:nucl-th/0609020 (2006)
49. C. Amsler et al., Phys. Lett. B **667**, 1 (2008). (Particle Data Group Collaboration)
50. D. Rein, L.M. Sehgal, Ann. Phys. **133**, 79 (1981)
51. D. Rein, Z. Phys. C **35**, 43 (1987)
52. K.S. Kuzmin, V.V. Lyubushkin, V.A. Naumov, Mod. Phys. Lett. A **19**, 2815 (2004). arXiv:hep-ph/0312107
53. K.S. Kuzmin, V.V. Lyubushkin, V.A. Naumov, Nucl. Phys. Proc. Suppl. **139**, 158 (2005). arXiv:hep-ph/0408106
54. A. Rodriguez et al., Phys. Rev. D **78**, 032003 (2008). arXiv:0805.0186 [hep-ex] (K2K Collaboration)
55. R.P. Feynman, M. Kislinger, F. Ravndal, Phys. Rev. D **3**, 2706 (1971)
56. K. Furuno et al., Prepared for 2nd International Workshop on Neutrino—Nucleus Interactions in the Few GeV Region (NUINT 02), Irvine, California, 12–15 Dec. 2002 (2003)
57. G. Ingelman, A. Edin, J. Rathsman, Comput. Phys. Commun. **101**, 108 (1997). arXiv:hep-ph/9605286
58. J.M. Levy, arXiv:hep-ph/0407371 (2004)
59. J.R. Ellis, A. Kotzinian, D.V. Naumov, Eur. Phys. J. C **25**, 603 (2002). arXiv:hep-ph/0204206
60. T. Sjostrand, arXiv:hep-ph/9508391 (1995)
61. T. Sjostrand, Comput. Phys. Commun. **39**, 347 (1986)
62. T. Sjostrand, M. Bengtsson, Comput. Phys. Commun. **43**, 367 (1987)
63. M. Gluck, E. Reya, A. Vogt, Eur. Phys. J. C **5**, 461 (1998). arXiv:hep-ph/9806404
64. C. Andreopoulos, Acta Phys. Polon. B **37**, 2349 (2006) (GENIE Collaboration)
65. K.S. Kuzmin, V.V. Lyubushkin, V.A. Naumov, arXiv:hep-ph/0511308 (2005)
66. K.S. Kuzmin, V.V. Lyubushkin, V.A. Naumov, Phys. At. Nucl. **69**, 1857 (2006)
67. L.J. Winton, Ph.D. Thesis, University of Melbourne (1999)
68. D. Rein, L.M. Sehgal, Nucl. Phys. B **223**, 29 (1983)
69. D. Rein, Nucl. Phys. B **278**, 61 (1986)
70. K. Hiraide et al., arXiv:0811.0369 [hep-ex] (SciBooNE Collaboration) (2008)
71. O. Benhar, A. Fabrocini, S. Fantoni, I. Sick, Nucl. Phys. A **579**, 493 (1994)
72. R.A. Smith, E.J. Moniz, Nucl. Phys. B **43**, 605 (1972)
73. S.A. Kulagin, R. Petti, Nucl. Phys. A **765**, 126 (2006). arXiv:hep-ph/0412425
74. G. Battistoni, P. Lipari, J. Ranft, E. Scapparone, arXiv:hep-ph/9801426 (1998)
75. J. Ranft, Z. Phys. C **43**, 439 (1989)
76. A. Ferrari, P.R. Sala, J. Ranft, S. Roesler, Z. Phys. C **70**, 413 (1996). arXiv:nucl-th/9509039
77. D. Casper, Nucl. Phys. Proc. Suppl. **112**, 161 (2002). arXiv:hep-ph/0208030
78. Q. Wu et al., Phys. Lett. B **660**, 19 (2008). arXiv:0711.1183 (NOMAD Collaboration)
79. E.A. Paschos, J.Y. Yu, M. Sakuda, Phys. Rev. D **69**, 014013 (2004). arXiv:hep-ph/0308130
80. A. Marchionni, M. Veltri, NOMAD internal memo 98-023 (1998)
81. B.D. Yabsley, NOMAD internal memo 97-028 (1997)
82. B.D. Yabsley, NOMAD internal memo 98-011 (1998)
83. A. Kayis-Topaksu et al., Eur. Phys. J. C **30**, 159 (2003) (CHORUS Collaboration)
84. P. Vilain et al., Phys. Lett. B **364**, 121 (1995)
85. R. Petti, arXiv:hep-ex/0411032 (NOMAD Collaboration) (2004)
86. V.V. Lyubushkin, B.A. Popov, Phys. At. Nucl. **69**, 1876 (2006)